# Hadronization within a Nambu–Jona-Lasinio model with a Polyakov loop

Eric Blanquier*
*12 Boulevard des capucines, F-11 800 Trèbes, France*
*and Université de Toulouse; UPS, 118 Route de Narbonne, F-31062 Toulouse, France*
(Received 6 August 2013; revised manuscript received 29 December 2013; published 11 June 2014)

I developed a dynamical model devoted to studying the cooling of a quark-antiquark plasma and its hadronization into mesons and baryons. To perform this modeling, I considered the Nambu–Jona-Lasinio (NJL) model, completed by the inclusion of a Polyakov loop, to form the PNJL model. I studied the mesonization, but also the baryonization of this system, thanks to cross sections calculated according to $\sqrt{s}$, the temperature, and the densities. In the performed simulations, I identified the dominant reactions. I also underlined the existence of a remote interaction between quarks. A purpose of this paper was to compare the NJL and PNJL results to see if one of these two models can make it possible to obtain a full hadronization of an open system initially composed of quarks and antiquarks.

DOI: 10.1103/PhysRevC.89.065204 PACS number(s): 11.10.Wx, 13.60.Le, 13.60.Rj, 25.75.Nq

## I. INTRODUCTION

Nowadays, the phase transition between the quark gluon plasma (QGP) and the hadronic matter is an intensely studied phenomenon, experimentally and theoretically. In the framework of experiments performed in the BNL Relativistic Heavy Ion Collider (RHIC) or in the CERN Large Hadron Collider (LHC), e.g., Ref. [1], we hope to have a better understanding of the involved physics. Moreover, the cooling of the QGP constitutes a fascinating challenge theoretically. It requires modeling the interaction between the interacting particles. It notably includes the estimation of the associated cross sections. However, the description of such physics appears as a rather delicate task because the associated QCD equations cannot be fully solved at the involved energies. Lattice QCD calculations [2–7] allow interesting progress in our knowledge of the quark physics. However, this approach showed its limitations to work at high baryonic densities because of the fermion sign problem [7,8].

At the same time, the Nambu–Jona-Lasinio model [9,10] proved its reliability to describe quark physics for a long time. This model was progressively improved by various developments since its creation. One can notably quote papers as Refs. [11,12] and [13–16], and then Refs. [17] and [18–21]. Some recent papers should also to be mentioned, such as Refs. [22,23]. About current evolutions, I mention, for example, the study of eight-quark interactions [24–28], proving that the model continues to be enhanced. Furthermore, thanks to the use of the Matsubara formalism [29], this approach is able to work at finite temperatures. Also, the model makes it possible to work at finite chemical potentials and therefore at finite densities [23]. The NJL approach considers that the interactions between quarks can be reduced to a punctual interaction [30], assumed by massive gluons. These ones are represented by scalar terms. So, they intervene by way of effective coefficients. In fact, the gluons do not really exist in the framework of the NJL model as dynamical degrees of freedom. The absence of confinement is an important consequence of this approximation. Also, the model is not renormalizable. In practice, this difficulty is solved by the use of a cutoff $\Lambda$ in the numerical calculations. The NJL model makes it possible to model effective *u,d,s* quarks, starting from their naked masses. Then, these effective quarks are usable to treat composite particles, such as mesons [17,31–33]. Furthermore, some approaches to describe baryons were also proposed, notably as a quark-diquark bound state [20,34–36]. In the framework of the NJL model, Refs. [37–47] can be considered as an overview of the baryon's modeling. Moreover, the NJL approach makes it possible to estimate the cross sections of reactions involving the evoked particles. So, quark-quark or quark-antiquark elastic scatterings were studied [48,49]. In the same way, inelastic reactions, such as mesonization processes $q + \bar{q} \rightarrow M + M$, were modeled in the NJL approach [32]. This work was followed by the analysis of meson-meson elastic scattering; see Refs. [50,51] or [52]. Then, some studies evoked the possibility to model processes involving diquarks and baryons [44,53]. As a whole, the NJL cross sections are estimated according to $\sqrt{s}$ and the temperature, as in Ref. [54]. However, the calculations can also be done at finite baryonic densities [55] and in the $T, \rho_B$ plane, i.e., at finite temperatures and densities in the same time [56]. Clearly, being aware of these qualities of the NJL approach, this model is often considered as a valuable tool to describe the hadronization of a quark-antiquark plasma.

In parallel, dynamical models were proposed in the framework of nuclear and particle physics. As indicated in Ref. [57], two types of approaches can be evoked: the macroscopic and the microscopic ones. Concerning the macroscopic models, one quotes the relativistic hydrodynamics [58–65] proposed in 1953 by Landau. This approach considers the matter as a continuous relativistic fluid. In an ideal fluid-dynamics description, the local thermodynamic equilibrium should be satisfied. As explained in Ref. [65], small departures from equilibrium are treatable by viscous fluid-dynamics approaches. In fact, experimental results, e.g., Ref. [66], go on the sense of a rapid thermalization of the QGP, leading to local equilibrium of the expanding fireball. Therefore, these observations validate a hydrodynamic description of this phase. Concerning the microscopic models, we notably have the ultrarelativistic

*ericblanquier@hotmail.com

 

quantum molecular dynamics (UrQMD) [57,67]. It considers covariant transport equations and interactions between particles are described via cross-section calculations. In practice, this model can be employed to describe the hadronic phase, e.g., Refs. [68,69].

Recent approaches can also be quoted, such as the parton hadron string dynamics (PHSD) [70–73] that solves a Boltzmann equation, the Boltzmann approach for multiparton scattering (BAMPS) [74], etc. Also, I mention works such as Refs. [75–77] that consider coalescence models and quark recombination to describe the formation of hadrons from quarks and gluons. Furthermore, we have Ref. [78], which uses a Boltzmann equation and studies the formation of mesons by quark-antiquark interactions. All the evoked models constitute a relevant starting point. Also, they can inspire some ideas in the framework of a dynamical model using NJL, such as the collision criterion evoked, e.g., in Ref. [67]. Some attempts were performed in this way [53,79,80] that used a molecular dynamics approach. In fact, two methods can be proposed. The first one studies the cooling of the quark-antiquark system by the use of an external thermostat. This one controls the progressive decrease in temperature according to time. This method seems to be adapted to describe the phase transition of systems considered as infinite. The second method [80] considers the notion of local parameters. The purpose is to study the mutual influence of the particles and to be able to describe local effects. The use of local parameters makes it possible to study, for example, core-corona interactions.

However, because of the absence of confinement in the NJL model, a quark can appear as free outside of the required conditions of the QGP. It can notably be true at the end of a cooling modeled by a pure NJL model. Of course, such an artifact appears as a strong limitation of the approach. A pure NJL description is maybe not sufficient to correctly describe the involved physics in such a work. To cure the absence of confinement, it was recently proposed to couple the quarks and antiquarks to a Polyakov loop [81–83]. It forms the Polyakov Nambu–Jona-Lasinio model (PNJL) [84–93]. It proposes a mechanism that simulates the confinement. This improvement of the model appears to be a very promising approach. I can mention, e.g., the behavior observed at low temperatures: This one is enhanced compared to a pure NJL model thanks to the suppression of the contribution of colored states on the thermodynamics [87,89]. Also, the inclusion of the Polyakov loop allows a more efficient restoration of the chiral symmetry, as observed in Ref. [91], by a strong decrease in the masses of the dressed quarks around the critical temperature. This behavior is in agreement with LQCD results, as noted in Ref. [88]. A good agreement between PNJL results and LQCD data was also reported in Refs. [86,93]. Moreover, in previous publications [45,94], I studied the possibility to adapt the modeling of the NJL particles in the framework of the PNJL description. It concerned the mesons, the diquarks, and the baryons. In the same way, I compared the cross sections calculated with the NJL and the PNJL models. I considered the processes quoted above, i.e., elastic reactions implying quarks/antiquarks, the mesonization reactions, and inelastic processes allowing the formation of diquarks or baryons. I found that the inclusion of the Polyakov loop leads to a shifting of the found values toward higher temperatures, compared to a pure NJL description. This remark concerns the particles' masses and the cross sections. However, at finite densities and low temperatures, it was reported in the literature the possible formation of a particular state associated with the color superconductivity phenomenon [95–100]. It needs a specific treatment, notably by using the Nambu-Gorkov formalism [95,96]. This aspect can be considered as a limitation of the domain of validity of models not using this formalism. However, as explained in Ref. [94], the temperature and density conditions required to study the cooling of a $q/\bar{q}$ plasma seem to be definitely outside of the domain in which the color superconductivity is expected to intervene. In contrast, cold and dense systems, such as the cores of neutron stars [98], seem to be concerned by the color superconductivity.

In fact, it could be interesting to investigate the influence of the Polyakov loop on the results found in the framework of a dynamical study. In other words, it could be studied how the modifications observed with the masses and the cross sections could affect the simulations. The amplitude of these modifications should be evaluated. Also, the characteristics of such an approach and its possible limitations should be stated. More precisely, we want to know if the confinement mechanism proposed by the PNJL model could be efficient enough to avoid free quarks in the end of the simulations. In addition, it seems to be well admitted that the cooling of a quark-antiquark system is dominated by a colossal mesonization. The strong cross sections of $q + \bar{q} \rightarrow M + M$ [32,54,94] confirm this hypothesis. The baryonization seems to be rather limited. Also, modest cross sections for processes that create baryons were observed [94]. In this reference, a scenario was proposed in which the baryonization should start after the mesonization. This hypothesis was justified while saying that the antiquarks must be consumed to form mesons to not interfere in the formation of the baryons. Indeed, the antiquarks can destroy the baryons via some inelastic reactions described in Ref. [94]. Therefore, the inclusion of the baryons in a dynamical evolution model could lead new elements of information to confirm the scenario or show its limitations. The role played by the diquarks is also to be highlighted. Even if they are not expected to be present in the end of the cooling, will they be produced in great quantities? Do they really contribute to the formation of the baryons? What are the dominant reactions that permit the baryonization?

To try to answer the questions formulated in the previous paragraph, I propose to organize the paper in the following way. In Sec. II, I perform a rapid description of the (P)NJL models. At this occasion, I recall some results associated with the treated PNJL particles by a study of their masses according to the temperature and/or the baryonic density. I also present some cross-section results involving these particles. Then, in Sec. III, I detail the algorithm devoted to the study, based, as in Ref. [80], on a relativistic molecular dynamics description. I propose there a comparison with other approaches, notably with Ref. [80], to explain my choices concerning some aspects of the implemented method. I indicate how one estimates the

external parameters used in the work, i.e., the temperature and the densities. Also, I describe the part of the algorithm devoted to the treatment of the collisions. I establish a list of all the included processes. About theoretical considerations, I also insist particularly on the equations of motion and the way to interpret and exploit them. In Sec. IV, some first results are shown. The purpose is to see some properties of the model and to underline relevant aspects. In this way, trajectories of particles are plotted and analyzed. The results obtained with complete simulations are gathered in Secs. V and VI. Section V focuses on a comparison between results found with the NJL approach and with the PNJL one. In Sec. VI, the evolution of relevant observables is presented. The objective is notably to understand the various phases of the cooling. One also finds the dominant reactions in these simulations.

TABLE I. NJL parameter sets. The masses and the cutoff are expressed in MeV, $G$, and $G_{\rm DIQ}$ are in MeV$^{-2}$. $K$ is in MeV$^{-5}$.

| Parameter set | $m_{0u}$ | $m_{0d}$ | $m_{0s}$ | Cutoff $\Lambda$ | $G\,\Lambda^2$ | $K\,\Lambda^5$ | $G_{\rm DIQ}$ |
|---|---|---|---|---|---|---|---|
| P1 | 4.75 | 4.75 | 147.0 | 708.0 | 1.922 | 10.00 | 0.705 $G$ |
| EB | 4.00 | 6.00 | 120.0 | 708.0 | 1.922 | 10.00 | 0.705 $G$ |

## II. THE POLYAKOV NAMBU–JONA-LASINIO MODEL

### A. The NJL approach

A first application of the NJL modeling concerns the calculations of the effective quark masses, starting from their naked masses $m_{0f}$. At finite temperature $T$ and densities $\rho_f$, the system of equations to be solved to find the mass $m_f$ of the $f$ flavor quark is [17,20,32]

$$\begin{aligned} m_f &= m_{0f} - 4G\langle\langle\bar\psi_f\psi_f\rangle\rangle + 2K\langle\langle\bar\psi_j\psi_j\rangle\rangle\langle\langle\bar\psi_k\psi_k\rangle\rangle\big|_{\substack{f=u,d,s\\ f\neq j \text{ and } f\neq k}} \\ \rho_f &= 2N_c\int\frac{d^3p}{(2\pi)^3}[f^+(\beta(E_f-\mu_f)) - f^-(\beta(E_f+\mu_f))]\Big|_{f=u,d,s}. \end{aligned} \tag{1}$$

The first line of Eq. (1) is the gap equation obtained while applying the mean-field approximation. The quark condensate of flavor $f$ is written as [49]

$$\langle\langle\bar\psi_f\psi_f\rangle\rangle = \frac{m_f\,N_c}{4\pi^2}A(m_f,\mu_f,\beta,\Lambda), \tag{2}$$

where $\psi_f$ refers to the field of flavor $f$ quarks, $N_c=3$ is the number of colors, $\beta=1/T$ is the inverse of the temperature, and $\mu_f$ is the chemical potential of the flavor $f$ quark. In Eq. (2), an $A$ function is used, associated with a one-fermion line integral. This function, extracted from Refs. [31,32] is defined as

$$A(m_f,\mu_f,\beta,\Lambda) = \frac{16\pi^2}{\beta}\sum_n\int\frac{d^3p}{(2\pi)^3}\frac{1}{(i\omega_n+\mu_f)^2-E_f^2}, \tag{3}$$

where $i\omega_n=(2n+1)\pi/\beta$ are fermionic Matsubara frequencies (uneven frequencies). I recall that bosonic Matsubara frequencies are even numbers [29,31]. $E_f=\sqrt{\vec p^{\,2}+m_f^2}$ is the energy of the quark. In the second line of Eq. (1),

$$f^\pm(\beta(E_f\mp\mu_f)) = \frac{1}{e^{\beta(E_f\mp\mu_f)}+1} \tag{4}$$

are the standard Fermi-Dirac distributions: $f^+$ concerns the quarks and $f^-$ the antiquarks. The coefficients that appear in Eq. (1) are listed in Table I. In this table, I mention the $G_{\rm DIQ}$ constant, which is used to model the diquarks. The cutoff $\Lambda$ corresponds to the upper bound of integrals, in the numerical calculations. The P1 parameter set is inspired from Refs. [44,53,54]. It uses the isospin symmetry: It implies that $m_u=m_d\equiv m_q$ and $\rho_u=\rho_d\equiv\rho_q$. This parameter set was used in this paper to recall some results obtained in Refs. [45,94]. They concern the masses of the quarks, mesons, diquarks, and baryons [45] and the cross sections of reactions involving these particles [94]. These data are reproduced in Secs. II C and II D, in which the baryonic density is expressed as $\rho_B=2/3\rho_q$ [21], with $\rho_s=0$. In the NJL literature, the parameter set proposed by Klevansky *et al.* [31,32,48] and used, e.g., in Ref. [80] could also be evoked. Compared to this one, P1 gives close results, notably with the light pseudoscalar mesons. The fact that P1 handles slightly heavier dressed quarks constitutes the main difference.

In Ref. [45], the parameter set named EB was introduced. It does not consider the isospin symmetry. It is used in all my dynamical simulations. Indeed, an objective of the approach is to be able to work under conditions for which the isospin symmetry is not necessarily verified. In heavy-ion collisions, the excess of neutrons over protons can lead to $\rho_d>\rho_u$, even if this asymmetry is negligible at top RHIC energies and at LHC. In Ref. [45], it was shown that EB and P1 give comparable results. However, the agreement between EB and experimental data is sometimes better, notably in the case of pseudoscalar and vectorial mesons.

### B. Inclusion of a Polyakov loop: The PNJL model

First, the inclusion of the Polyakov loop affects the grand potential expression [83,91], written as

$$\begin{aligned} \Omega_{\rm PNJL} &= \mathcal{U}(T,\Phi,\bar\Phi) + 2G\sum_{f=u,d,s}\langle\langle\bar\psi_f\psi_f\rangle\rangle^2 - 4K\langle\langle\bar\psi_u\psi_u\rangle\rangle\langle\langle\bar\psi_d\psi_d\rangle\rangle\langle\langle\bar\psi_s\psi_s\rangle\rangle \\ &\quad - 2N_c\sum_{f=u,d,s}\int_0^\Lambda\frac{p^2\,dp}{2\pi^2}\left\{E_f + \frac{T}{N_c}\mathrm{Tr}_c\ln[Z_\Phi^+(E_f)] + \frac{T}{N_c}\mathrm{Tr}_c\ln[Z_\Phi^-(E_f)]\right\}. \end{aligned} \tag{5}$$

Compared to the pure NJL one, the effective potential $\mathcal{U}$ is added [83]. As in Refs. [85,88,91], I consider

$$\frac{\mathcal{U}(T,\Phi,\bar{\Phi})}{T^4} = -\frac{a\,(T)}{2}\,\Phi\bar{\Phi} + b(T)\,\ln[1 - 6\Phi\bar{\Phi} + 4(\Phi^3 + \bar{\Phi}^3) - 3(\Phi\bar{\Phi})^2], \tag{6}$$

with

$$a\,(T) = a_0 + a_1\left(\frac{T_0}{T}\right) + a_2\left(\frac{T_0}{T}\right)^2 \quad \text{and}$$

$$b(T) = b_3\left(\frac{T_0}{T}\right)^3. \tag{7}$$

The coefficients used in Eq. (7) are gathered in Table II [88,91].

$\Phi$ and $\bar{\Phi}$ are, respectively, the expectation value of the Polyakov field and its conjugate. They are defined by $\Phi\,(\vec{x}) = \frac{\mathrm{Tr}_c\langle\langle L(\vec{x})\rangle\rangle}{N_c}$ and $\bar{\Phi}(\vec{x}) = \frac{\mathrm{Tr}_c\langle\langle L^\dagger(\vec{x})\rangle\rangle}{N_c}$, where

$$L\,(\vec{x}) = \mathcal{P}\exp\left[i\int_0^\beta A_4\,(\vec{x},\tau)\;d\tau\right] \tag{8}$$

designates the Polyakov line. Also, $\mathcal{P}$ is a path ordering operator and $A_4$ is the temporal component of the Euclidian gauge field [83,87,89,91]. In the framework of the mean-field approximation, $\Phi$ and $\bar{\Phi}$ are real numbers. They are considered as independent variables in the calculations [88]. Indeed, they are not equal [8] in the general case.

Another consequence of the inclusion of the Polyakov loop is the adaptation of the partition functions $Z^{\pm}(E_f) = 1 + e^{-\beta\,(E_f \mp \mu_f)}$ that become [83,87,92]

$$\begin{aligned} Z^+_\Phi(E_f) &= 1 + Le^{-\beta\,(E_f-\mu_f)},\\ Z^-_\Phi(E_f) &= 1 + L^\dagger e^{-\beta\,(E_f+\mu_f)}. \end{aligned} \tag{9}$$

$Z^+_\Phi$ is associated with quarks and $Z^-_\Phi$ with antiquarks. These modifications imply an update of the Fermi-Dirac distributions [89,91], because there are calculated by

$$f^{\pm}_\Phi(\beta(E_f \mp \mu_f)) = \pm\frac{1}{\beta}\,\frac{\partial\left[\frac{1}{N_c}\mathrm{Tr}_c\ln(Z^{\pm}_\Phi)\right]}{\partial\mu_f}, \tag{10}$$

which leads to

$$\begin{aligned} &f^+_\Phi(\beta(E_f-\mu_f))\\ &\quad= \frac{(\Phi + 2\bar{\Phi}\;e^{-\beta(E_f-\mu_f)})e^{-\beta(E_f-\mu_f)} + e^{-3\beta(E_f-\mu_f)}}{1 + 3(\Phi + \bar{\Phi}e^{-\beta(E_f-\mu_f)})e^{-\beta(E_f-\mu_f)} + e^{-3\beta(E_f-\mu_f)}},\\ &f^-_\Phi(\beta(E_f+\mu_f))\\ &\quad= f^+_\Phi(\beta(E_f-\mu_f))|_{\Phi\leftrightarrow\bar{\Phi},\;\mu_f\leftrightarrow-\mu_f}. \end{aligned} \tag{11}$$

As indicated in Ref. [89], in the PNJL calculations, this update concerns all the equations in which Fermi-Dirac distributions associated with quarks/antiquarks are employed, as, e.g., Eq. (1).

TABLE II. PNJL parameters.

| $a_0$ | $a_1$ | $a_2$ | $b_3$ | $T_0$ |
|---|---|---|---|---|
| 3.51 | –2.47 | 15.2 | –1.75 | 270 MeV |

Moreover, because of the inclusion of $\Phi$ and $\bar{\Phi}$ in the grand potential (5), two extra equations are added to the system to be solved Eq. (1) [87,91]:

$$\frac{\partial\Omega_{\mathrm{PNJL}}}{\partial\Phi} = 0, \quad \frac{\partial\Omega_{\mathrm{PNJL}}}{\partial\bar{\Phi}} = 0. \tag{12}$$

The purpose of Eq. (12) is to minimize the grand potential according to $\Phi$ and $\bar{\Phi}$. In the framework of the PNJL model, for a given temperature $T$ and for densities $\rho_f$, the system of Eqs. (1) and (12) makes it possible to estimate the masses of the quarks $m_f$, their associated chemical potentials $\mu_f$, and the values of the Polyakov fields $\Phi$ and $\bar{\Phi}$.

### C. Order parameters and particle masses in the (P)NJL models

The NJL model makes it possible to study the restoration of the chiral symmetry, by means of the chiral condensate introduced in Eq. (2), used as an order parameter. In the framework of the mean-field approximation, the dressed quarks result from a coupling of the naked quarks with the chiral condensates, Eq. (1). With the PNJL model, the quarks are also coupled to the Polyakov loop $\Phi$. This one is another order parameter associated with the phase transition between the "confined" phase and the "deconfined" one. I use quotation marks because they correspond to pure gauge calculations, as recalled in Ref. [89]. The denomination is conserved, however, when quarks are added in the modeling.

The numerical solutions of Eqs. (1) and (12) make it possible to estimate the values of these order parameters. The evolution of the light quark condensate is presented in Fig. 1(a). I normalized the results by the value of the condensate at null temperature and null densities. With the P1 parameter set (solid line), $\langle\langle\bar{\psi}_u\psi_u\rangle\rangle = \langle\langle\bar{\psi}_d\psi_d\rangle\rangle \equiv \langle\langle\bar{\psi}_q\psi_q\rangle\rangle$, whereas for EB (dashed line), I plotted $1/2\,(\langle\langle\bar{\psi}_u\psi_u\rangle\rangle + \langle\langle\bar{\psi}_d\psi_d\rangle\rangle)$. In agreement with the (P)NJL literature, the restoration of the chiral symmetry is performed by way of a crossover because $m_{0f} \neq 0$ (Table I). One also confirms that the inclusion of the Polyakov loop leads to increase the value of the pseudocritical temperature $T_c$ of this crossover [83]. One has $T_c \approx 230$ MeV for a pure NJL description, versus $T_c \approx 270$ MeV in the PNJL one. These results concern P1 and EB: The curves associated with these parameter sets are very close. In Fig. 1(b), I plotted the values of the Polyakov field $\Phi$ according to the temperature and the baryonic density. $\Phi$ increases when the temperature is growing. According the PNJL literature, e.g., Ref. [91], it can be recalled that $\Phi \approx \bar{\Phi} \to 0$ corresponds to the "confined" regime, whereas $\Phi \approx \bar{\Phi} \to 1$ corresponds to the "deconfined" one.

Equations (1) and (12) also lead to the quark masses published in Ref. [45] and reproduced in Fig. 2. This one allows a comparison with the NJL quark masses presented in Ref. [18]. The NJL and the PNJL models strictly coincide at null temperature, whatever the densities. The results are also comparable at high temperatures ($T > 400$ MeV). Moreover,

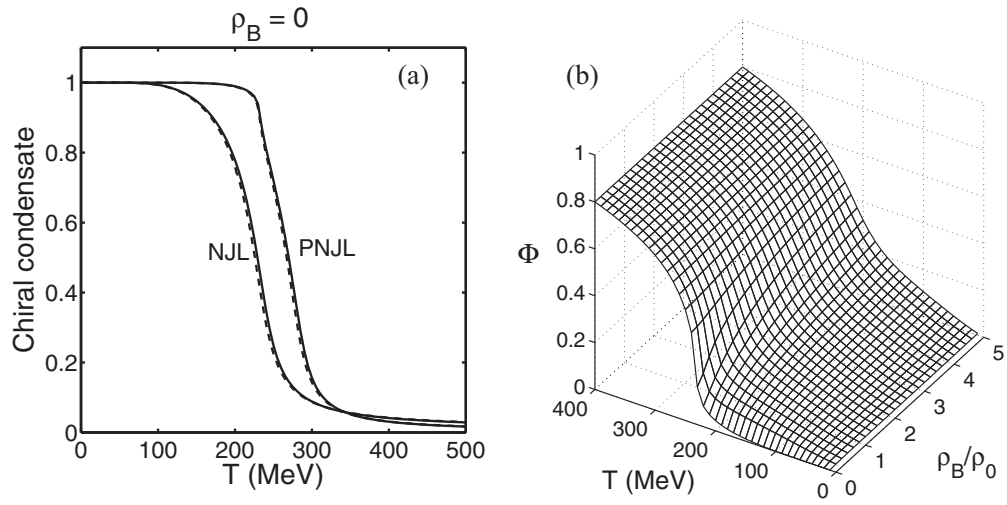


FIG. 1. (a) Evolution of the light quark condensate according to the temperature; the solid line refers to P1 and the dashed line to EB. (b) Evolution of the Polyakov loop $\Phi$ in the $T,\rho_B$ plane, extracted from Ref. [45].

the evolution of the light quark masses presents strong similarities with the one of their chiral condensates, Fig. 1(a), explainable with the gap equation (1).

About the modeling of composite particles built with quarks and/or antiquarks, one only needs to adapt the quark/antiquark Fermi-Dirac distributions with Eq. (11) to take into account the inclusion of the Polyakov loop [89,91]. The modeling of mesons, diquarks, and baryons is performed by solving equations whose structure is schematically similar. For a composite particle at rest, we have [45]

$$\det[1 - \mathcal{Z}\ \Pi(k_0,\vec{k})] = 0|_{k_0=M,\|\vec{k}\|=0}, \tag{13}$$

where $M$ is the mass of the studied particle.

Concerning the mesons, $\Pi$ is the irreducible polarization function. It represents a quark-antiquark loop. $\Pi$ is defined as [17,32]

$$-i\,\Pi^{\Gamma}_{q_1\bar{q}_2}(i\nu_m,\vec{k}) = N_C \frac{i}{\beta}\sum_n \int \frac{d^3p}{(2\pi)^3}\mathrm{Tr}[iS_{f_1}(i\omega_n,\vec{p}) \times \Gamma\, iS_{f_2}(i\omega_n - i\nu_m,\vec{p}-\vec{k})\Gamma], \tag{14}$$

in which $S_f$ is the flavor $f$ quark propagator in momentum space [88]:

$$S_{f\,\mathrm{NJL}}(\not{p}) = \frac{i}{\not{p} + \gamma_0\,\mu_f - m_f} \quad \text{and}$$
$$S_{f\,\mathrm{PNJL}}(\not{p}) = \frac{i}{\not{p} + \gamma_0(\mu_f - iA_4) - m_f}. \tag{15}$$

With the pseudoscalar mesons, $\Gamma = i\gamma_5$. Concerning the scalar mesons, used as propagators in the cross-section calculations, $\Gamma$ is the $4\times 4$ identity matrix $1_4$. The $\mathcal{Z}$ term in Eq. (13) is equal to $4K^{\pm}_{ii}$, where $i$ depends on the treated meson [17,32]. The plus sign refers to pseudoscalar mesons; the minus is for scalar ones. For example, with $\pi^{\pm}$,

$$K^{+}_{11} = G + \tfrac{1}{2}N_C\ K\ i\ \mathrm{Tr}[\tilde{S}_s(x,x)], \tag{16}$$

where $\mathrm{Tr}[\tilde{S}_f(x,x)]$ is the trace of the quark propagator expressed in coordinate space [32]. In the framework of the isospin symmetry, the pseudoscalar mesons $\eta,\eta'$ are coupled; idem for the scalar mesons $f_0, f_0'$. In these cases, the procedure

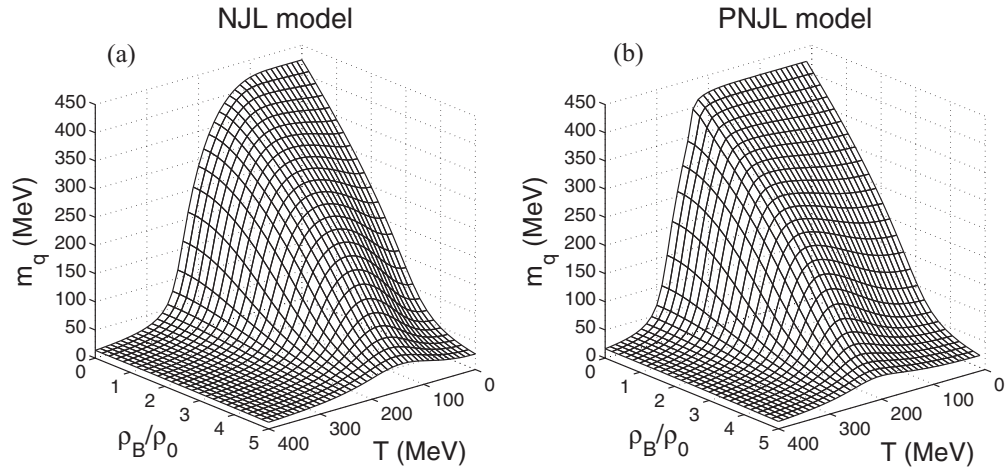


FIG. 2. Light quark mass according to the temperature and the baryonic density, with $\rho_0 \approx 0.16\,\mathrm{fm}^{-3}$, in the (a) NJL and (b) PNJL models.

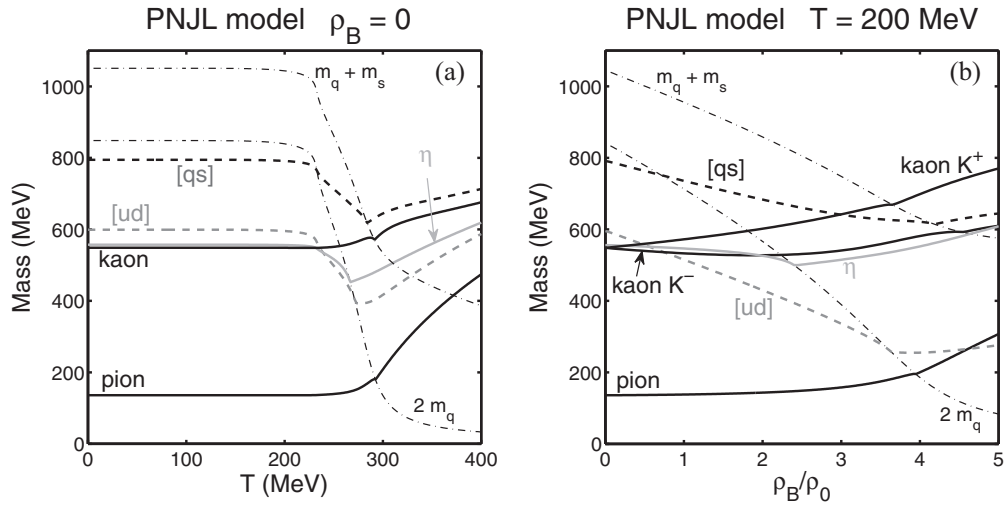


FIG. 3. Masses of pseudoscalar mesons and scalar diquarks according to (a) the temperature and (b) the baryonic density.

is detailed in Ref. [32]. When the isospin symmetry is not applied, $\pi_0$ is coupled to $\eta, \eta'$. It requires an extension of the applied method [45].

Concerning the diquark [44,45,53,101], the $\Pi$ function can be expressed by

$$-i\,\Pi^{\Gamma}_{q_1q_2}(i\nu_m,\vec{k}) = \frac{i}{\beta}\sum_n\int\frac{d^3p}{(2\pi)^3}\mathrm{Tr}[iS_{f_1}(i\omega_n - i\nu_m,\vec{p}-\vec{k}) \times \Gamma\, iS^{\mathcal{C}}_{f_2}(i\omega_n,\vec{p})\Gamma], \quad (17)$$

in which $S^{\mathcal{C}}_f$ is the propagator of a charge conjugate quark, obtained by reversing the sign of $\mu_f$ in Eq. (15). The $\Pi$ term translates a loop formed by a quark and a charge conjugate antiquark. This one mimics the behavior of a quark, to obtain with Eqs. (13) and (17) the expected description of a diquark. Because of the charge conjugation operator $\mathcal{C} = i\gamma_0\gamma_2$ [18], $\Gamma = i\gamma_5$ for scalar diquarks, and $\Gamma = 1_4$ for pseudoscalar ones. Here, $\mathcal{Z} = 2\,G_{\mathrm{DIQ}}$ [45] (Table I).

About the baryons, I model these particles as the association of a quark and a diquark [44,45,53]. By the use of the static approximation [39,45,53], one comes back to the structure of Eq. (13). In this case, the $\Pi$ function describes a loop formed by a quark and a charge conjugate diquark, or a loop using a diquark and a charge conjugate quark. It leads, e.g., to

$$-i\,\Pi(i\nu_m,\vec{k}) = \frac{i}{\beta}\sum_n\int\frac{d^3p}{(2\pi)^3}\mathrm{Tr}\big[iS_q(i\omega_n,\vec{p}) \times iS^{\mathcal{C}}_D(i\omega_n - i\nu_m,\vec{p}-\vec{k})\big], \quad (18)$$

where, $S^{\mathcal{C}}_D$ is the propagator of a charge conjugate diquark. The $\mathcal{Z}$ term is written as

$$\mathcal{Z} = g\;g'\;F\;F'\left(-\frac{i}{m}\right), \quad (19)$$

where $m$ is the mass of the exchanged quark. The $g$ are coupling constants and the $F$ gathers color and flavor factors [45]. With baryons as $\Lambda$, several states are considered, i.e., $[ud]+s$,

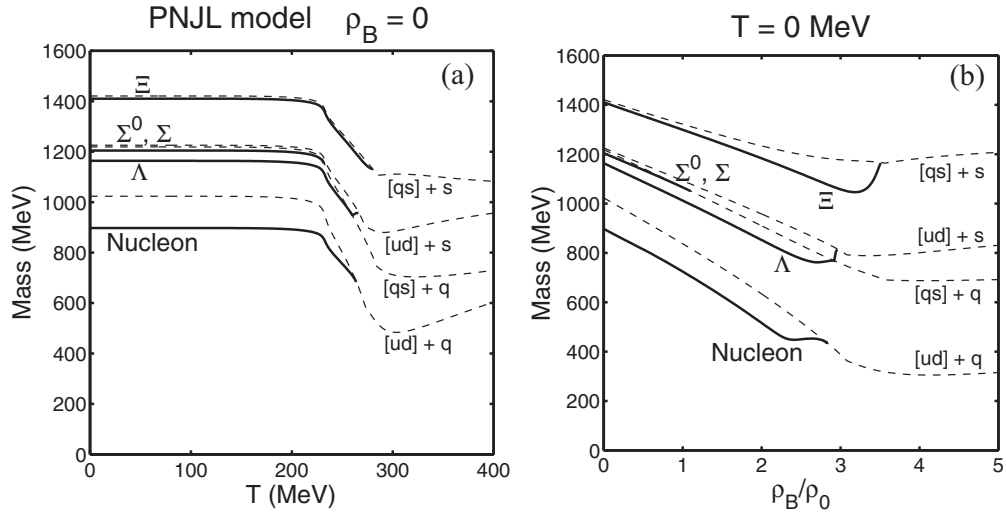


FIG. 4. Masses of the octet baryons according to (a) the temperature and (b) the baryonic density.

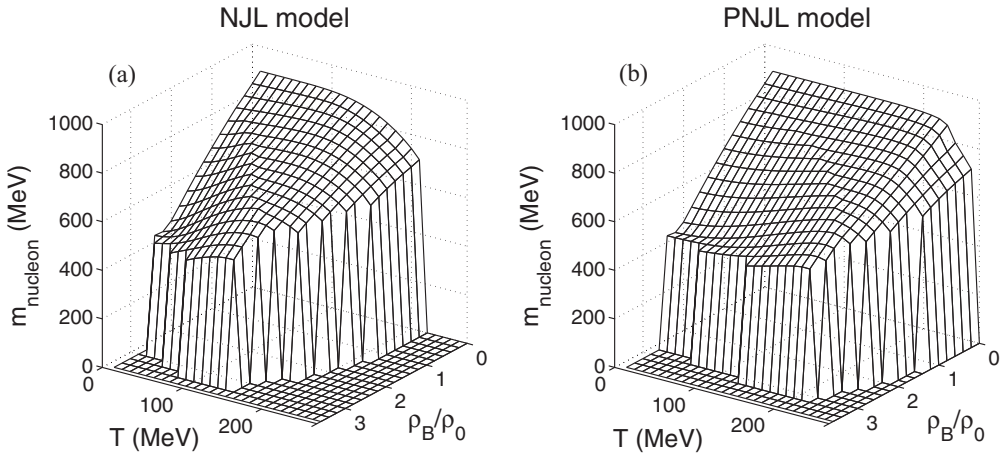


FIG. 5. Mass of the nucleon in the $T-\rho_B$ plane, in the (a) NJL and (b) PNJL models.

$[us]+d$, and $[ds]+u$. In these cases, Eq. (13) is still valid, but $\Pi$ and $\mathcal{Z}$ are now matrices [44,45].

Some results extracted from Refs. [45,94] are reproduced in Figs. 3–5. In my dynamical model, the considered composite particles are the pseudoscalar mesons (but not $\eta'$), the scalar diquarks $[ud]$, $[us]$, $[ds]$, and the octet baryons. In Fig. 3, I also plotted the curves "$2m_q$" and "$m_q+m_s$" associated with the masses of the quarks/antiquarks that compose the mesons and diquarks. The purpose is to see when these composite particles are lighter or heavier than the quarks/antiquarks that compose them. In the first case, the particle is stable. In the second case, the particle can disintegrate into a $q,\bar{q}$ pair (meson) or a quark pair (diquark). In Fig. 3(a), the Mott temperature, or critical temperature, materializes the frontier between these two regimes. The NJL and PNJL values are indicated in Table III. In comparison with Fig. 1(a), the Mott temperatures are roughly around the pseudocritical temperature $T_c$.

### D. (P)NJL cross sections calculations

#### 1. General formulas

In this paper, I consider collisions involving two incoming particles, labeled as 1 and 2, and two outgoing ones, labeled 3 and 4. The Eq. (20) is used to evaluate the cross sections associated with these collisions, in the center-of-mass reference frame of the two incoming particles [32],

$$\sigma(\sqrt{s},T,\rho_f) = [1 \pm f_{F,B}(\beta(E_3^* \mp \mu_3))] \times [1 \pm f_{F,B}(\beta(E_4^* \mp \mu_4))] \int_{t_-}^{t_+} dt \frac{\partial\sigma}{\partial t}, \quad (20)$$

TABLE III. Mott temperatures, in MeV, of the mesons and diquarks in the (P)NJL models, with P1.

| Model | Pion | Kaon | $\eta$ | $[ud]$ | $[qs]$ |
|---|---|---|---|---|---|
| NJL | 246 | 245 | 216 | 223 | 238 |
| PNJL | 292 | 292 | 267 | 272 | 284 |

where

$$\frac{\partial\sigma}{\partial t} = \frac{1}{64\pi\ s\ (\vec{p}_1^{\,*})^2} \frac{1}{4N_c^2} \sum_{s,c} |\mathcal{M}|^2 \quad (21)$$

is the differential cross section according to the Mandelstam variable $t$ (Appendix B). In Eq. (21), $\mathcal{M}$ is a matrix element obtained by a summation of the existing channels, i.e., $s$, $s'$, $t$, $u$ ... Then, this term is summed upon the spins and the colors $s$, $c$. In Eq. (20), the terms placed in front of the integral translate the fact that particles 3 and 4 are produced in a medium in which other identical particles are already present. In the case of fermions, these terms are named *Pauli blocking factors* [48,67] and take the form $1-f_F$. More precisely, $f_F$ is the Fermi-Dirac distribution, Eq. (4), updated with Eq. (11) in the case of PNJL quarks/antiquarks [94]. In the case of bosons [32], $1+f_B$ is considered, where $f_B$ is the Bose-Einstein distribution. Moreover, Eq. (20) explicitly mentions the dependence of $\sigma$ according to $\sqrt{s}$, but also according to $T$ and $\rho_f$. Indeed, the masses of the involved particles and the propagators depend on these parameters. So, $\mathcal{M}$ and $\frac{\partial\sigma}{\partial t}$ depend on them [94]. Moreover, the chemical potentials $\mu$ that appear in the mentioned terms are solutions of Eqs. (1) and (12), in which $T$ and $\rho_f$ are used as parameters.

Concerning the inelastic processes listed in Sec. III C 2, each reaction type is included with its reverse process, e.g., $q+\bar{q} \to M+M$ with $M+M \to q+\bar{q}$. In fact, the matrix elements used in Eq. (20) are time-reversal invariant, in agreement with the detailed balance principle [67]. So, compared to a direct reaction, the estimation of a reverse reaction only requires to change $\vec{p}_1^{\,*2}$ in Eq. (21) by $\vec{p}_3^{\,*2}$ and to replace the blocking factors associated with particles 3 and 4 with the ones of particles 1 and 2, as explained in Ref. [94]. Thus, if one labels $i \to f$ a reaction and $f \to i$ its reverse reaction, one arrives at the relation between their associated cross sections,

$$\sigma_{f\to i} = \frac{(\vec{p}_i^{\,*})^2}{(\vec{p}_f^{\,*})^2} \frac{F_i}{F_f} \sigma_{i\to f}, \quad (22)$$

in which $\vec{p}_i^{\,*} \equiv \vec{p}_1^{\,*}$, $\vec{p}_f^{\,*} \equiv \vec{p}_3^{\,*}$. Moreover, $F_i \equiv [1 \pm f_{F,B}(\beta\ (E_1^* \mp \mu_1))]\ [1 \pm f_{F,B}(\beta\ (E_2^* \mp \mu_2))]$ and

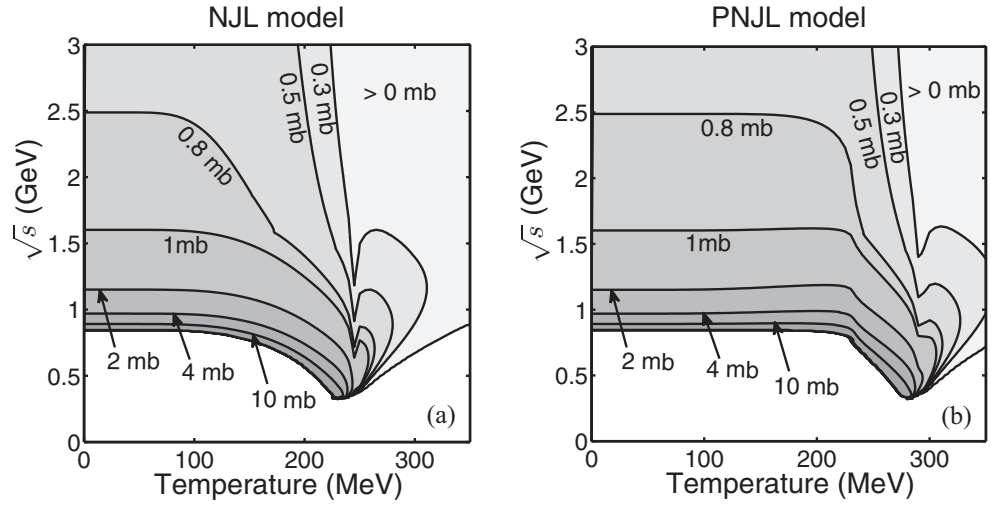


FIG. 6. Cross sections of $u + \bar{u} \to \pi^+ + \pi^-$ in the $T, \sqrt{s}$ plane, for $\rho_B = 0$, in the (a) NJL and (b) PNJL models.

$F_f \equiv [1 \pm f_{F,B}(\beta\,(E_3^* \mp \mu_3))]\,[1 \pm f_{F,B}(\beta\,(E_4^* \mp \mu_4))]$. Clearly, the Eq. (22) presents strong similarities with the one presented in Refs. [57,67] when the application of the detailed balance principle in the UrQMD collisions was discussed.

#### 2. *Overview of some (P)NJL results*

The mesonization reactions $q + \bar{q} \to M + M$ were proposed by Ref. [32] and considered, e.g., in Ref. [54]. (P)NJL results, presented in Ref. [94], are reproduced in Fig. 6. As noted in these references, the cross sections can be strong, locally exceeding 100 mb at the level of the kinematic threshold defined as

$$\sqrt{s}_{\text{threshold}} = \max[(m_1 + m_2),(m_3 + m_4)], \tag{23}$$

where $m_i$ are the masses of the incoming/outgoing particles. More precisely, a divergence at the threshold is observed when $T \leqslant 230\,\text{MeV}$ in the NJL model, versus $T \leqslant 280\,\text{MeV}$ in the PNJL one. At these limit temperatures, the cross sections have optimal values near the threshold. These temperatures are comparable to $T_c$ [Fig. 1(a)]. The Mott temperature of the pions (Table III) is slightly stronger in the two models. On the graphs, it corresponds to the temperature for which the "0.3 mb" curve appears as a "V". Before this temperature, $u + \bar{u} \to \pi^+ + \pi^-$ is *exothermic* [32]; i.e., $m_1 + m_2 > m_3 + m_4$. It becomes endothermic after this temperature and the divergence at the threshold totally disappears.

Inelastic reactions using diquarks and/or baryons were studied with the PNJL model [94]. It was reported that the diquark production is expected to be weak. Indeed, the reactions producing diquarks present weak cross sections. The best candidate to allow this production seems to be $q + q \to D + M$, but under some conditions: moderate temperatures and $\rho_B$ higher than $\rho_0$ (Fig. 7). At null density, the reaction studied in this figure is exothermic until a temperature close to 240 MeV in the PNJL model. The other reaction types that can produce diquarks are endothermic [94].

In Ref. [94], I found that the cross sections associated with baryonization reactions are definitely lower than the ones of the mesonization process. Three dominant reaction

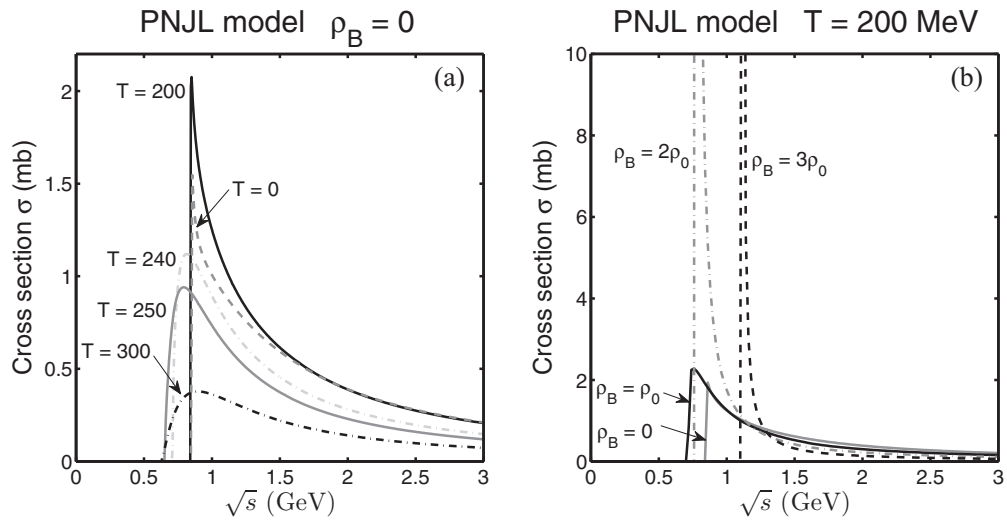


FIG. 7. Cross sections of $u + d \to [ud] + \pi^0$, according to (a) the temperature and (b) the baryonic density.

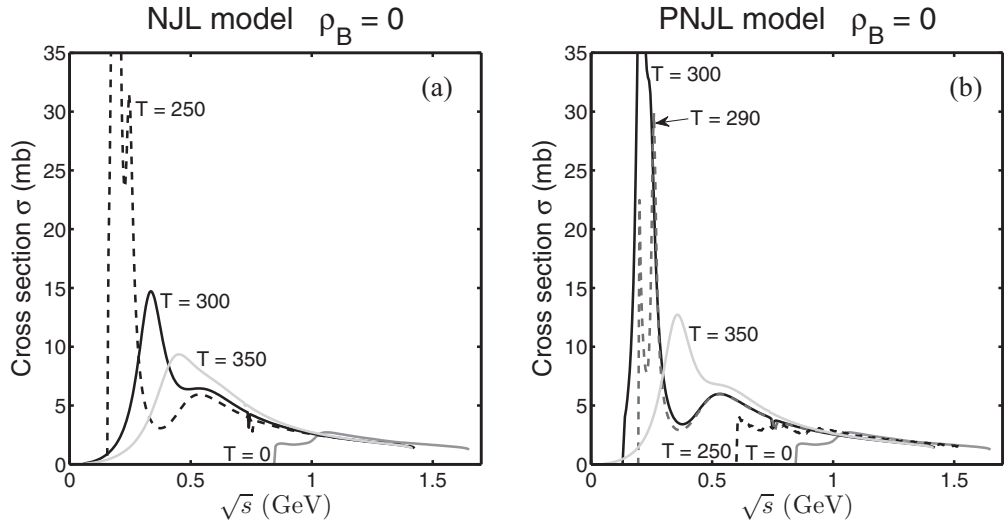


FIG. 8. Cross sections of $u + \bar{u} \to u + \bar{u}$ in the (a) NJL and (b) PNJL models.

types were identified: $D + D \to B + q$, $q + D \to M + B$, and $q + q \to B + \bar{q}$. In the reactions involving light particles, $q + D \to M + B$ and $q + q \to B + \bar{q}$ can present cross sections close to 1 mb, whereas $D + D \to B + q$ can exceed 4 mb near the kinematic threshold, at low temperatures and densities. However, $D + D \to B + q$ requires an important population of diquarks, at the opposite of $q + q \to B + \bar{q}$. Also, $q + D \to M + B$ has the advantage to form observable particles starting from nonobservable ones, e.g., during the last phases of the cooling. Moreover, these three processes are endothermic. It includes reactions involving nucleons. Indeed, at null temperature and density, each of the momenta $\|\vec{p}_1^*\|$ and $\|\vec{p}_2^*\|$ of the incoming particles must be greater than 500 MeV for $u + u \to p + \bar{d}$, 270 MeV for $[ud] + [ud] \to p + d$, and 70 MeV for $u + [ud] \to \pi^+ + n$ ($p$, proton; $n$, neutron). The momenta of the particles are linked to the temperature. So, reactions as $u + u \to p + \bar{d}$ are expected to intervene at higher temperatures than the two other ones.

Among the elastic reactions, the ones involving quarks and/or antiquarks appear to be the most important during the evolution of the quark-antiquark plasma. Indeed, such reactions play a great role in the thermalization of the initial $q/\bar{q}$ plasma. Furthermore, elastic reactions are often concurrent of inelastic ones, notably $q + \bar{q} \to q + \bar{q}$ with $q + \bar{q} \to M + M$. However, the elastic process is expected to occur at slightly higher temperatures than the inelastic one, i.e., about 20 MeV above. This remark is true in the NJL model [48,49] and in the PNJL one [94] (Fig. 8). In fact, as noted in Ref. [48], the optimal temperature of $u + \bar{u} \to u + \bar{u}$ is very close to the Mott temperature of the pion, used in this reaction as propagator.

### 3. *Extra calculations of some cross sections*

In this paper, I added the elastic processes $q + M \to q + M$, $\bar{q} + D \to \bar{q} + D$, $q + D \to q + D$, $\bar{q} + B \to \bar{q} + B$, $q + B \to q + B$ and the ones that concern their associated antiparticles: $\bar{q} + M \to \bar{q} + M$, etc. Notably, I described $q + M \to q + M$ by means of a $t$ channel in which a quark is exchanged. It leads to cross sections of a few barns for the reaction $u + \pi^0 \to u + \pi^0$. Concerning, e.g., $q + B \to q + B$, I considered the $t$ channel described in Fig. 9 and Eq. (24), in which $\mathcal{D}_t$ is the (P)NJL propagator of the exchanged diquark. The associated results are presented in Fig. 10 for $u + p \to u + p$. The found values are not negligible. They exceed 10 mb at reduced temperature, lower than 200 MeV, and at low densities, i.e., $\rho_B < 0.5\rho_0$. About the elastic processes involving two composite particles, I mention, e.g., $D + B \to D + B$, treated by a $t$ channel involving an exchanged quark. It leads to cross sections exceeding 7 mb only at the level of the kinematic threshold, at moderate temperatures, $T \approx 200$ MeV, and $\rho_B \approx 2\rho_0$,

$$-i\mathcal{M}_t = f_t \bar{u}(p_4)\, u(p_2) i\mathcal{D}_t(p_3 - p_1)\bar{u}(p_3)\, u(p_1). \qquad (24)$$

Other possibilities also concern $M + D \to M + D$, $D + D \to D + D$, etc. These reactions types are treatable with the method explained in Refs. [50,51]. It can also be used for the modeling of $M + M \to M + M$. However, to describe this process, I considered the formulas established in Ref. [57]. This remark is also valid for $M + B \to M + B$ or $B + B \to B + B$.

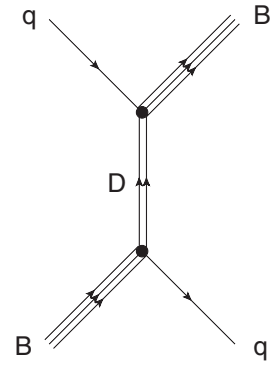


FIG. 9. $t$ channel for $q + B \to q + B$.

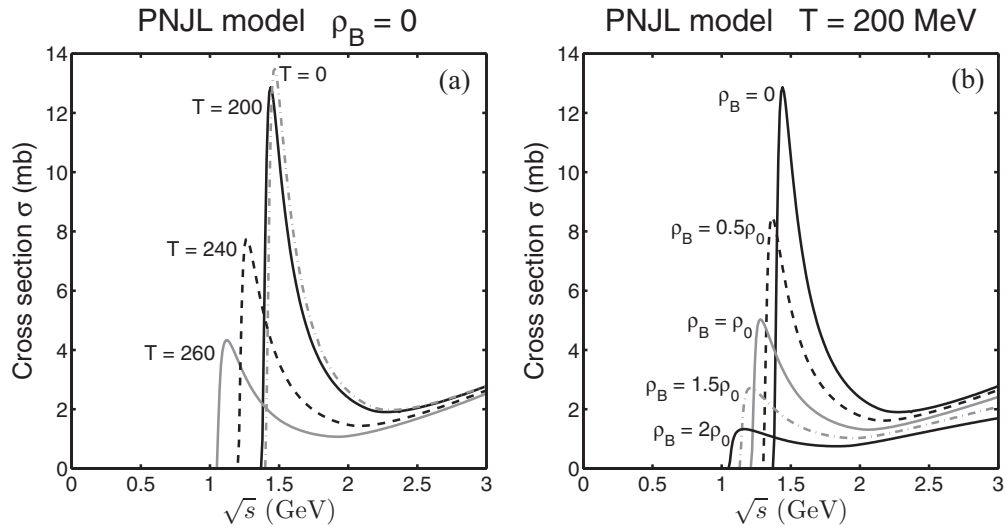


FIG. 10. Cross sections of $u + p \to u + p$, according to (a) the temperature and (b) the baryonic density.

## III. DESCRIPTION OF THE ALGORITHM

### A. The global algorithm

In the framework of the works presented in this paper, a stand-alone computer program was developed. The program, and by extension the algorithm, can be designated by the software's unofficial name, i.e., ARCHANGE. This name does not correspond to an acronym. The global algorithm is not really different compared to the ones described in the literature, as, e.g., Refs. [53,80]. Indeed, I consider the following steps, which are described in more detail in Secs. III B, III C, and III D.

(i) *System initialization.* In this step, the initial particles are created and added into the system, while defining their positions and momenta. Then, the program determines the environment of each particle. More precisely, it calculates the values of the external parameters $(T, \rho_f)$ in the vicinity of each particle. This procedure makes it possible to calculate the initial mass of each of them.

(ii) *Treatment of the collisions.* In this step, one investigates all the possibility of collisions between each possible couple of particles. The applied collisions are determined by the program. This one treats then the replacement of the particles in the system when required.

(iii) *Treatment of the movements.* Here, one applies equations of motion to periodically update the position and the momentum of each particle.

(iv) Return to point (ii) for the next time iteration until the end of the simulation.

More precisely, for each quark/antiquark present in the system, one determines the local external parameters $T, \rho_f$ felt by the particle. These parameters are imposed to the particle by the other ones present in its vicinity. In the NJL model, its mass and its chemical potential are estimated when one solves Eq. (1). In the PNJL model, Eqs. (1) and (12) also supply the values of $\Phi$ and $\bar{\Phi}$. As a consequence, the temporal evolution of these values is ruled by the evolution of the external parameters and therefore by the close environment of the studied particle. This procedure is performed regularly for each quark/antiquark to take into account the evolution of its environment, notably in the framework of points (ii) and (iii). The method is similar for the composite particles, i.e., mesons, diquarks, and baryons. Indeed, Eqs. (1) and (12) are solved in the same way, and then the found data (masses of the quarks ...) are used in Eq. (13) associated with the studied composite particle.

Equations (1) and (12) were established in the framework of the mean-field approximation. It wants to say that this approach requires that the thermodynamic equilibrium is established. The external parameters are estimated locally; thus, we consider local thermodynamic equilibrium. It imposes low variations of the measured temperatures and densities, according to distance and time. It was checked in the simulations described hereafter that these constraints were verified. Furthermore, low variations of $T, \rho$ necessarily lead to low variations of $\Phi$ [Fig. 1(b)]. Such a behavior is indeed expected because $\Phi$ is the *average* of the Polyakov loop.

Moreover, as indicated in the Introduction, the thermalization of the QGP phase is expected to be very rapid. As a consequence, how a quark system evolves towards kinetic and chemical equilibrium is an important question, which is investigated, e.g., in Refs. [102–105]. Notably, the papers [102,103] consider simulations in a box to study the evolution of quark/gluon systems. It is particularly pointed out the contributions of multiparticle reactions as $2 \to 3$ and $3 \to 2$. More precisely, Refs. [102,103] indicate that gluon multiplication $g + g \to g + g + g$ leads to the chemical equilibrium and to a rapid kinetic equilibration. In my description, the gluons and these multiparticle reactions are not included. However, we will see if the simulations can reach kinetic and chemical equilibrium.

### B. Determination of the external parameters

The external parameters $T, \rho_f$ are evaluated for each particle in the laboratory frame of reference. One considers that

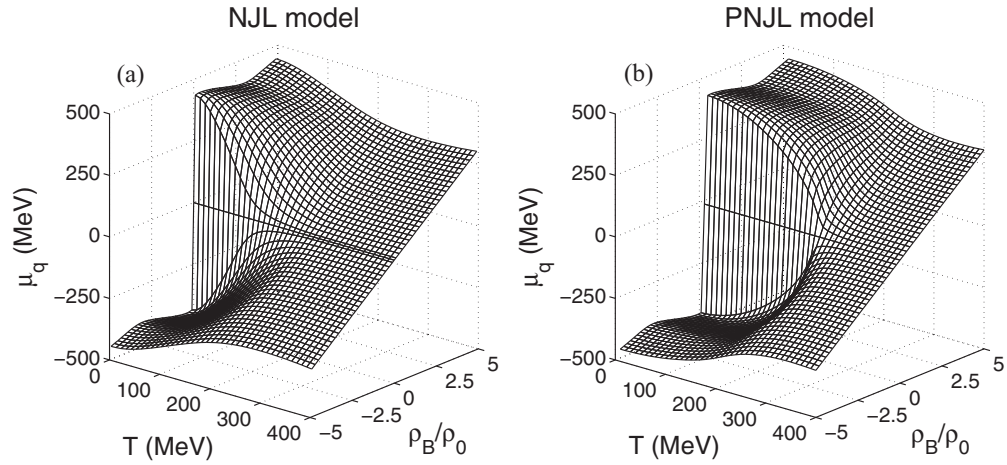


FIG. 11. Chemical potential $\mu_q$ according to $\rho_B$ and $T$, in the (a) NJL and (b) PNJL models.

this reference frame always coincides with the center-of-mass reference frame of the whole system. *Stricto sensu*, it can be noted in Eq. (13) that the particle's momentum modulus $k$ should be treated as an external parameter for the composite particles (external because $k$ is evaluated in the laboratory reference frame). However, the influence of $k$ on the particle's mass is rather negligible, especially in the $k$ domain used in this work.

#### 1. The densities

About the densities $\rho_f$, my choice to consider them is different from the one of Ref. [80]. In fact, we observe in Fig. 11, extracted from Ref. [45], that the relation between $\rho_B$ and $\mu_q$ ($q \equiv u,d$) is not obvious in the (P)NJL models. More precisely, $\mu_q$ is a function of $\rho_B$ but also of the temperature $T$, especially at low temperatures. Clearly, this remark also concerns the chemical potentials $\mu_f$ with the associated $\rho_f$ and $T$.

The density $\rho_f$ felt by the $i$ particle is determined by the formula

$$(\rho_f)_i = \frac{1}{V} \sum_{j \neq i} w(i,j)[(n_f)_j - (n_{\bar{f}})_j], \tag{25}$$

where $V$ is the volume of a sphere centered on the studied particle $i$. This fictitious sphere defines the vicinity of the particle. The $j$ summation in Eq. (25) is performed upon the particles forming the system. Also, $(n_f)_j$ and $(n_{\bar{f}})_j$ designate, respectively, the number of flavor $f$ quarks and antiflavor $\bar{f}$ antiquarks "contained" in particle $j$. For example, with a proton, $n_u = 2$, $n_{\bar{u}} = 0$, $n_d = 1$, $n_{\bar{d}} = 0$, $n_s = 0$, and $n_{\bar{s}} = 0$. To take into account the distance $d_{ij}$ between the $i$ and $j$ particles, a coefficient is applied during the counting. This coefficient is supplied by a *weighting function*. As in Ref. [80] in which such a function was used, this one is defined here as

$$w(i,j) = \exp\left(-\frac{d_{ij}^2}{2D^2}\right). \tag{26}$$

$D$ is linked to the sphere radius. In practice, I chose $D =$ 1.75 fm in most of the numerical calculations.

#### 2. The temperature

The determination of the temperature felt by each particle is far from being trivial. In Ref. [80], a relation was established between the densities and the temperature. In my approach, temperature and densities are treated as independent parameters, without correlation between them.

In statistical physics, the use of the equipartition theorem is a relevant approach to estimate the temperature. In our case, complications come to the adaptation of this theorem to the relativistic regime and the necessity to work at thermal equilibrium. About the relativistic treatment, some approaches were proposed to introduce the notion of relativistic temperature [106–113]. Following the method proposed by Ref. [113], one writes

$$\left\langle \frac{(\vec{p})^2}{2E} \right\rangle = \frac{3}{2} k_B T, \tag{27}$$

in which $k_B$ is the Boltzmann constant, set to 1 in my work. $\langle\rangle$ is an averaging operator. In practice, this operation is performed on the momentum $\vec{p}$ and on the energy $E$ of the particles located in the vicinity of the studied particle $i$. As with the densities, the weighting function Eq. (26) is included in this calculation. The notion of local temperature is used in the description. So, local thermal equilibrium is expected, as explained in Sec. III A. Some extra explanations about the establishment of Eq. (27) are proposed in Appendix A.

### C. Treatment of the collisions

#### 1. Description of the employed method

First, one considers a particle in particular, labeled with $i$ in the explanations. Then one establishes a list of the couples that can be formed using this particle $i$ and all the ones present in its vicinity, labeled with $j$. Each couple $(i,j)$ represents a possibility of incoming particles that can interact. The particles' momenta are expressed in the laboratory reference frame in the data manipulated by the program. The (P)NJL cross sections available in the literature, and by extension the ones calculated in my description, are estimated in the center-of-mass reference frame of the two incoming particles $(i,j)$. As a consequence, a Lorentz boost is applied to these particles.

TABLE IV. List of reactions when a $u$ quark interacts with a $\bar{u}$ antiquark.

| Reaction type | Detail on the possible reactions | | |
|---|---|---|---|
| $q+\bar{q}\to q+\bar{q}$ | $u+\bar{u}\to u+\bar{u}$ | $u+\bar{u}\to d+\bar{d}$ | $u+\bar{u}\to s+\bar{s}$ |
| $q+\bar{q}\to M+M$ | $u+\bar{u}\to \pi^0+\pi^0$ | $u+\bar{u}\to \pi^0+\eta$ | $u+\bar{u}\to \eta+\eta$ |
| | $u+\bar{u}\to \pi^+ +\pi^-$ | $u+\bar{u}\to K^+ +K^-$ | |
| $q+\bar{q}\to D+\bar{D}$ | $u+\bar{u}\to [ud]+\overline{[ud]}$ | $u+\bar{u}\to [us]+\overline{[us]}$ | |

For each couple $(i,j)$, the impact parameter $b^*_{i,j}$ is estimated. Some couples can be invalidated if the particles are moving away or if the impact parameter is too high. Also, an extrapolation of the trajectories is performed to validate the couple $(i,j)$ only if the distance between $i$ and $j$ is minimal. It follows the idea evoked in Ref. [80].

For each remaining couple $(i,j)$, a sublist of the reaction types that can occur between $i$ and $j$ is established. Collisions involving two outgoing particles are considered. For each reaction type, the algorithm foresees the possible outgoing particles creatable by the reactions. Table IV proposes a list in the case of a quark/antiquark couple $(u,\bar{u})$. About $q+\bar{q}\to M+M$, reactions involving $\eta'$ are not considered. Indeed, they lead to negligible cross sections in front of the mesonization reactions that create light mesons, such as pions [32].

At this stage of the procedure, the cross sections of all the listed reactions are estimated. For each couple $(i,j)$ and for each reaction, labeled with $k$, the obtained cross section $\sigma_{i,j,k}$ is compared to the impact parameter $b^*_{i,j}$ of the couple. More precisely, the collision criterion mentioned in Refs. [57,67] is applied. It stipulates that a reaction is possible if its cross section satisfies the inequality

$$b^*_{i,j}\leqslant\sqrt{\sigma_{i,j,k}/\pi}. \tag{28}$$

Among all the reactions that verify this criterion, the program chooses the reaction $k$ associated with the couple $(i,j)$ that will be considered. This choice is determined in a stochastic way, but the probability of each reaction $(i,j,k)$ is weighted by its cross section. In other words, the reaction that has the strongest cross section at this moment is the one that has the strongest chance to occur.

Once the reaction and the associated couple are determined, i.e., it was found that particle $j$ will react with particle $i$ thanks to the reaction $k$, the scattering angle and the momenta of the outgoing particles are calculated. When the outgoing particles are inserted into the system, their masses are beforehand estimated in the conditions $(T,\rho_f)$ felt by the incoming particles $(i,j)$ before their replacement. The formulas used to treat the collisions are relatively standard and are gathered in Appendix C. Whatever reaction occurred, the new particles will no longer be able to interact before the next iteration. This is done to avoid that the same particles interact indefinitely together during the same iteration. Finally, the program considers then another particle $i$, and proceeds again as explained in this Sec. III C1, until all the particles are reviewed.

#### 2. Calculation of the cross sections

Table V gathers all the reaction types included in the modeling. An important number of possible reactions is to be considered, especially because my dynamical simulations do not apply the isospin symmetry. The included particles are the quarks $q$, the pseudoscalar mesons $M$, the scalar diquarks $D$, the octet baryons $B$, and their associated antiparticles. Furthermore, the cross sections depend on $\sqrt{s}$, the temperature $T$, and the densities (Sec. II D). As a consequence, the use of precalculated values is not the best solution, e.g., by using a cross sections database as in Ref. [80]. Certainly, this solution could be applied, but at the price of too-strong approximations. Indeed, for example, with $q+\bar{q}\to M+M$, a strong mesonization is expected, but in some precise $\sqrt{s}$, $T$, $\rho_f$ conditions [94]. This aspect is crucial in the study of the plasma's cooling. So, in my description, the cross sections are *real time* calculated: They are estimated when the program requires them, taking into account $\sqrt{s}$ and the particles' environment, via $T$ and $\rho_f$.

### D. Equations of motion

In a dynamical study involving quarks, relativistic effects cannot be neglected. So, this aspect must appear explicitly in the modeling, especially in the equations of motion. In the description, I consider a relativistic molecular dynamics description, whose equations of motion are similar to the ones mentioned, e.g., in Ref. [80]:

$$\begin{aligned}\frac{d\left(r_i^\mu\right)}{d\tau}&=\frac{p_i^\mu}{E_i},\\ \frac{d\left(p_i^\mu\right)}{d\tau}&=-\sum_{j\neq i}\frac{m_j}{E_j}\frac{\partial m_j}{\partial r_{i\,\mu}}.\end{aligned} \tag{29}$$

In these equations, $E$ is the energy of the concerned particle. As mentioned in Ref. [80], the writing of the second equation of Eq. (29) is justified by the fact that we do not have an explicit potential in the NJL model. This remark can be extended to the PNJL approach. However, the mass of each particle depends on parameters such as temperature and densities. In addition, we saw that these parameters are calculated for each particle via its vicinity, i.e., the other particles. Therefore, it is possible to consider that the potential is "hidden" in the particles' masses. The $\sum_{j\neq i}\frac{m_j}{E_j}\frac{\partial m_j}{\partial r_{i\,\mu}}$ term is thus interpretable as a remote interaction between the particles. According to Ref. [80], the derivative $\frac{\partial m_j}{\partial r_{i\,\mu}}$ can be developed as

$$\frac{\partial m_j}{\partial r_{i\,\mu}}=\frac{\partial m_j}{\partial T_j}\frac{\partial T_j}{\partial r_{i\,\mu}}+\sum_{f=u,d,s}\frac{\partial m_j}{\partial \rho_{f_j}}\frac{\partial \rho_{f_j}}{\partial r_{i\,\mu}}. \tag{30}$$

Nevertheless, I give another interpretation to this term. I say that it represents the variations of the masses of the particles $j$ induced by the position variation of particle $i$. In fact, the

TABLE V. List of the reaction types included in the model.

| Incoming particles | Possible reaction types | | |
|---|---|---|---|
| $q+\bar{q}$ | $q+\bar{q}\to q+\bar{q}$ | $q+\bar{q}\to M+M$ | $q+\bar{q}\to D+\bar{D}$ |
| $q+q$ | $q+q\to q+q$ | $q+q\to M+D$ | $q+q\to\bar{q}+B$ |
| $\bar{q}+\bar{q}$ | $\bar{q}+\bar{q}\to\bar{q}+\bar{q}$ | $\bar{q}+\bar{q}\to M+\bar{D}$ | $\bar{q}+\bar{q}\to q+\bar{B}$ |
| $q+M$ | $q+M\to q+M$ | $q+M\to\bar{q}+D$ | |
| $\bar{q}+M$ | $\bar{q}+M\to\bar{q}+M$ | $\bar{q}+M\to q+\bar{D}$ | |
| $\bar{q}+D$ | $\bar{q}+D\to\bar{q}+D$ | $\bar{q}+D\to q+M$ | $\bar{q}+D\to\bar{D}+B$ |
| $q+\bar{D}$ | $q+\bar{D}\to q+\bar{D}$ | $q+\bar{D}\to\bar{q}+M$ | $q+\bar{D}\to D+\bar{B}$ |
| $q+D$ | $q+D\to q+D$ | $q+D\to M+B$ | |
| $\bar{q}+\bar{D}$ | $\bar{q}+\bar{D}\to\bar{q}+\bar{D}$ | $\bar{q}+\bar{D}\to M+\bar{B}$ | |
| $\bar{q}+B$ | $\bar{q}+B\to\bar{q}+B$ | $\bar{q}+B\to q+q$ | $\bar{q}+B\to M+D$ |
| $q+\bar{B}$ | $q+\bar{B}\to q+\bar{B}$ | $q+\bar{B}\to\bar{q}+\bar{q}$ | $q+\bar{B}\to M+\bar{D}$ |
| $q+B$ | $q+B\to q+B$ | $q+B\to D+D$ | |
| $\bar{q}+\bar{B}$ | $\bar{q}+\bar{B}\to\bar{q}+\bar{B}$ | $\bar{q}+\bar{B}\to\bar{D}+\bar{D}$ | |
| $M+M$ | $M+M\to M+M$ | $M+M\to q+\bar{q}$ | |
| $M+D$ | $M+D\to M+D$ | $M+D\to q+q$ | $M+D\to\bar{q}+B$ |
| $M+\bar{D}$ | $M+\bar{D}\to M+\bar{D}$ | $M+\bar{D}\to\bar{q}+\bar{q}$ | $M+\bar{D}\to q+\bar{B}$ |
| $M+B$ | $M+B\to M+B$ | $M+B\to q+D$ | |
| $M+\bar{B}$ | $M+\bar{B}\to M+\bar{B}$ | $M+\bar{B}\to\bar{q}+\bar{D}$ | |
| $D+\bar{D}$ | $D+\bar{D}\to D+\bar{D}$ | $D+\bar{D}\to q+\bar{q}$ | |
| $D+D$ | $D+D\to D+D$ | $D+D\to q+B$ | |
| $\bar{D}+\bar{D}$ | $\bar{D}+\bar{D}\to\bar{D}+\bar{D}$ | $\bar{D}+\bar{D}\to\bar{q}+\bar{B}$ | |
| $\bar{D}+B$ | $\bar{D}+B\to\bar{D}+B$ | $\bar{D}+B\to\bar{q}+D$ | |
| $D+\bar{B}$ | $D+\bar{B}\to D+\bar{B}$ | $D+\bar{B}\to q+\bar{D}$ | |
| $D+B$ | $D+B\to D+B$ | | |
| $\bar{D}+\bar{B}$ | $\bar{D}+\bar{B}\to\bar{D}+\bar{B}$ | | |
| $B+\bar{B}$ | $B+\bar{B}\to B+\bar{B}$ | | |
| $B+B$ | $B+B\to B+B$ | | |
| $\bar{B}+\bar{B}$ | $\bar{B}+\bar{B}\to\bar{B}+\bar{B}$ | | |

displacement of a particle leads to perturbations in its vicinity. First, the densities felt by the other particles are modified, especially for the ones in its close neighborhood. Second, the displacement also induces a modification of the local temperature felt by these particles. These two effects are explainable by the method I use to estimate the densities and the temperature, especially via the use of a weighting function, Eq. (26). More precisely, every displacement induces a variation of the values returned by this function. It leads to modifications in the counting and thus it affects the $T,\rho_f$ values. The masses of the particles are calculated while using the temperature and the densities. Thus, it explains why the displacement of one particle is able to modify the masses of the other particles.

About the temperature, this parameter depends on the particles' energies, i.e., the momenta, but also the masses. The masses depend on the temperature. Therefore, there is interdependence between mass and temperature. This aspect is treated numerically by means of successive iterations until reaching convergence. The conservation of total energy and total momenta are two constraints imposed to the algorithm during this procedure.

## IV. SOME PRELIMINARY RESULTS

### A. The (P)NJL remote interaction

I propose to numerically investigate the properties of the previously described remote interaction. More precisely, I performed simulations, with the NJL and PNJL models, involving two $u$ quarks. In each simulation, the initial momenta were directed in opposite directions, but with $\|\vec{p}\| =$ 30 MeV for the two quarks. A "background temperature" $T =$ 200 MeV is imposed to simulate the conditions of hot systems. It implies that the temperature felt by the quarks is constant and Eq. (27) is not used. This use of background temperatures only concerns the results described in this Sec. IV A, but not the other simulations treated in this paper. In the test, the collision procedure is disabled. The obtained trajectories in the laboratory reference frame are presented by the form of chronograms in Fig. 12. Obviously, I remark that the notion of trajectories concerns classical motions. It thus constitutes a limitation of my description of the quark physics. The part of each trajectory that has the darkest tone corresponds to the more recent quark positions. It was verified that the total energy, the total momentum, and the angular momentum are conserved for each simulation time.

In Fig. 12, the obtained results show a remote interaction between the quarks. This interaction is attractive. This behavior is explained by the second equation of Eq. (29). A general tendency is that a particle modifies its trajectory to tend to minimize the masses of the particles located in its vicinity. Therefore, the two quarks are mutually attracted. Indeed, for a quark $j$, the approach of another quark $i$ induces an increase in the temperature and densities felt by $j$. Therefore, the mass of the quark $j$ decreases (Fig. 2). The same reasoning is valid

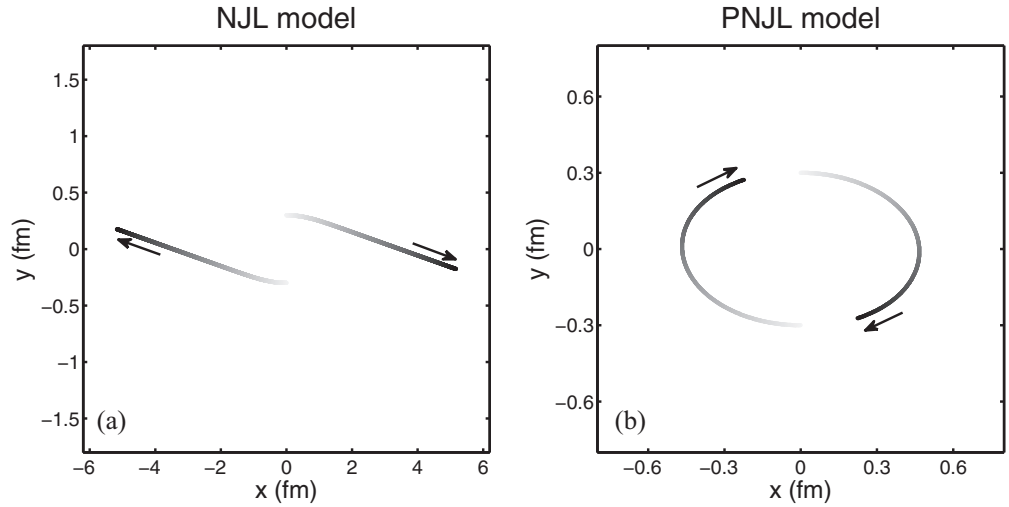


FIG. 12. Comparison of the results found with the (a) NJL and (b) PNJL models, with $T = 200$ MeV.

for the quark $i$ submitted to the action of the quark $j$ in a symmetric way. In the case of the simulations described in this Sec. IV A, because of the use of a background temperature, the evolution of the masses is only attributable to the density variations induced by the quarks.

Through this example, one interprets the $-\sum_{j\neq i} \frac{m_j}{E_j} \frac{\partial m_j}{\partial r_{i\,\mu}}$ term in the second line of Eq. (29) as a force. The remote interaction is clearly nonlinear: If one multiplies the number of quarks, the attractive effect is not necessarily multiplied by the same factor. It should be seen as an $N$-body interaction. Furthermore, the observed interaction has a limited range, in opposition with the QCD quark-quark potential. The (P)NJL remote interaction is strongly linked to the $T, \rho_f$ variations induced by the particles. As a consequence, the weighting function Eq. (26) plays a great role in the behavior of this interaction, especially in its range. The (P)NJL models appear to be able to mimic short-range phenomena described by QCD, but present limitations to modeling long-range ones. Moreover, the masses of the quarks tend towards their naked values ($m_{0f}$) at high temperatures and densities (Fig. 2). In this case, the mass of a quark is no longer influenced by $T, \rho_f$, i.e., by the environment. It coincides with the asymptotic freedom phenomenon, treated by the perturbative QCD.

The graphs of Fig. 12 show that the PNJL remote interaction is more intense than the NJL one in this test. Now I extend the analysis to other conditions to see if this observation can be generalized. The objective is to investigate the influence of the background temperature and the initial momentum of the quarks. In Fig. 13, one varies the applied temperature in the (P)NJL models. In these graphs, the initial momenta are fixed to $\|\vec{p}\| = 30$ MeV. I plotted the distance between one quark and the center of the system. The distance between the two quarks is found by applying a factor of two, thanks to the symmetry of the system. With the NJL model, Fig. 13(a) shows that the quarks stay together, as in Fig. 12(b), until a temperature close to 150 MeV. Indeed, in this regime, the

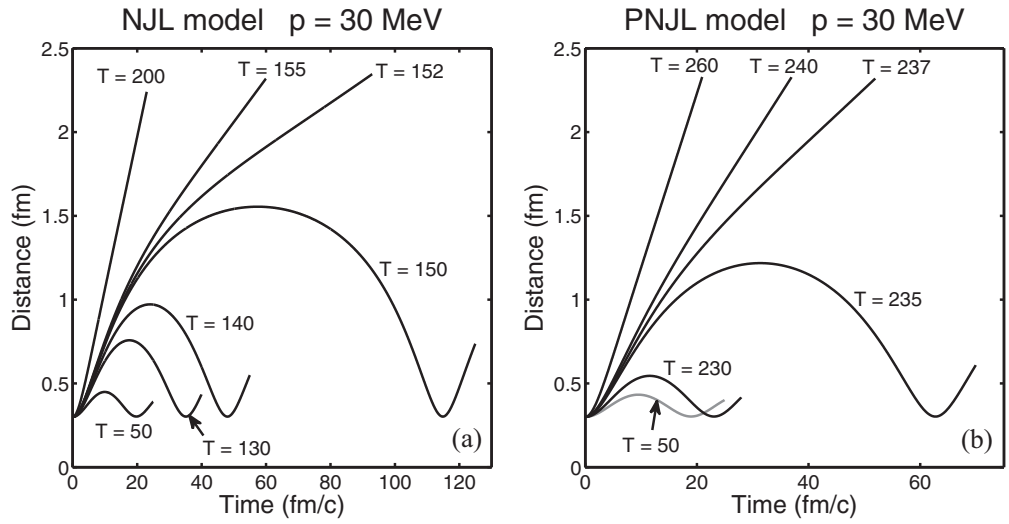


FIG. 13. Evolution of the distance between one quark and the center of the system, according to time, for $\|\vec{p}\| = 30$ MeV and at several temperatures (in MeV), in the (a) NJL and (b) PNJL models.

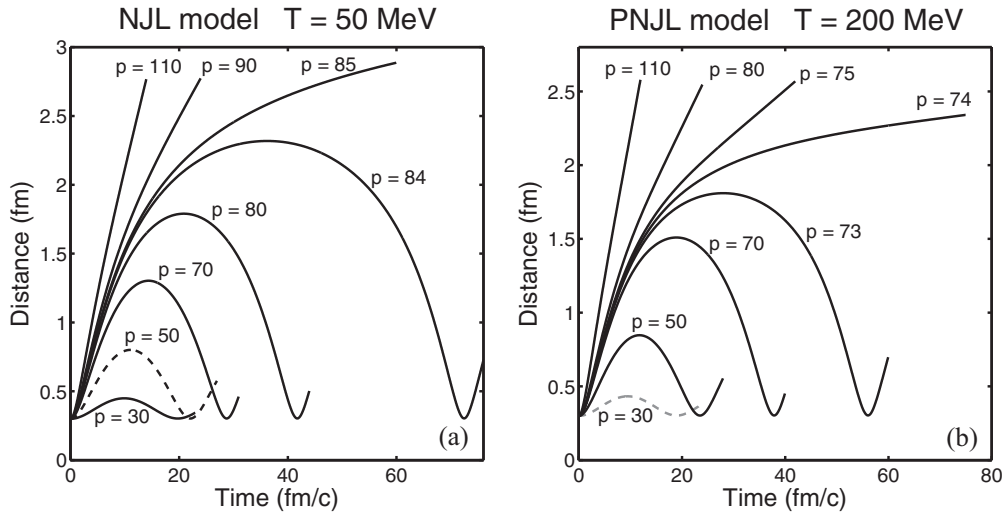


FIG. 14. Evolution of the distance between one quark and the center of the system, according to time, for several initial momenta (in MeV), in the (a) NJL and (b) PNJL models.

observed motion is periodic. However, when the temperature is growing, the amplitude of the motion increases, until this limit temperature. After this one, the force is not intense enough: The quarks are separated, as in Fig. 12(a). Concerning the PNJL model [Fig. 13(b)], the amplitude of the motion stays rather constant until $T = 230$ MeV. Then it strongly increases for higher temperatures. The limit temperature is close to 235 MeV in this case: It is largely higher than the one found with NJL.

This behavior is explainable by Fig. 2. In these tests, we saw that the remote interaction is related to the mass variations according to $\rho_f$ ($\rho_u$ more precisely). The quarks evolve in a $T, \rho_f$ zone in which the densities are low. In this zone, at modest temperatures, the derivative of the mass with respect to the density is strong. As remarked in Ref. [45], the effect of the Polyakov loop upon the quark masses is to shift the observed values towards higher temperatures, applying a distortion effect on the curves. At reduced densities, it implies that the zone for which $\frac{\partial m}{\partial \rho_f}$ is important is wider in the PNJL model than in the NJL one. Indeed, one finds, respectively, $T < 220$ MeV against $T < 150$ MeV in Fig. 2, in agreement with the results of Fig. 13. Beyond these temperatures, the reduction of $\frac{\partial m}{\partial \rho_f}$ leads to the observed weakening of the force owing to the density variations.

In fact, even if the simulations performed in this Sec. IV A do not include the contribution of the temperature variations on the force, the aspect of the graphs presented Fig. 2 suggests that these variations do not strongly intervene at modest temperatures, where $\frac{\partial m}{\partial T}$ is weak. At the opposite, this contribution could be more present just after the limit temperatures we saw upstream. More precisely, it is expected to be greater in the PNJL model than in the NJL one, because of the strong $\frac{\partial m}{\partial T}$ values visible in Fig. 2(b) when $220\,\text{MeV} < T < 280\,\text{MeV}$, at low densities. As a consequence, the domain in which the remote interaction is not negligible could be extended compared to the results of Fig. 13, notably with PNJL. In the case of this model, these speculations are verified in Sec. IV B, in which simulations are performed at $T \approx 260$ MeV, obviously without the use of a background temperature. More precisely, the remote interaction observed in Sec. IV B comes from the temperature variations caused by the studied quarks. During the cooling of a quark system, the found results showed that the attractive effect can be more present, i.e., act for a wider temperature range, thanks to the inclusion of the Polyakov loop. They lead us to imagine a provisory collapse of the quark system, which could optimize the hadronization processes, especially in the PNJL description.

However, the data presented in Figs. 12 and 13 concern very slow quarks: These results cannot be generalized. In Fig. 14, the influence of the initial momentum is studied. I consider two regimes. In Fig. 14(a), one works at rather low temperatures, i.e., 50 MeV, with the NJL model. In fact, PNJL results are very similar at this temperature. In Fig. 14(b), one considers an intermediate temperature, 200 MeV, with the PNJL model. The two figures show that the quarks stay together until a limit value of the initial momentum: $\|\vec{p}\| = 84$ MeV in Fig. 14(a) and $\|\vec{p}\| = 73$ MeV in Fig. 14(b), i.e., slow quarks in these two configurations. A few MeV above these limit values, the quarks are deviated by the force, but they do not stay together. As a consequence, Figs. 13 and 14 seem to indicate the existence of a "bound line" in the $T, p$ plane that marks the limit between the "bound" and "unbound" states. Obviously, this line strongly depends on the initial conditions of the modeled system, as, e.g., the initial distance between the quarks.

### B. Relativistic Brownian motion?

If we consider the remote interaction highlighted in Sec. IV A and the collisions, it is interesting now to see if there is a dominant behavior between them. In other words, if the collisions largely rule the dynamics, the system can maybe show a behavior close to the one of a relativistic Brownian motion [112]. At the opposite, if the remote interaction is strong enough, it might induce the collapse motion previously evoked. To answer this question, I perform a PNJL simulation. I gather 6 $u$ quarks and 6 $d$ quarks in a cube of size 2 fm, in the conditions of a hot and dense system. Indeed, 12 light quarks

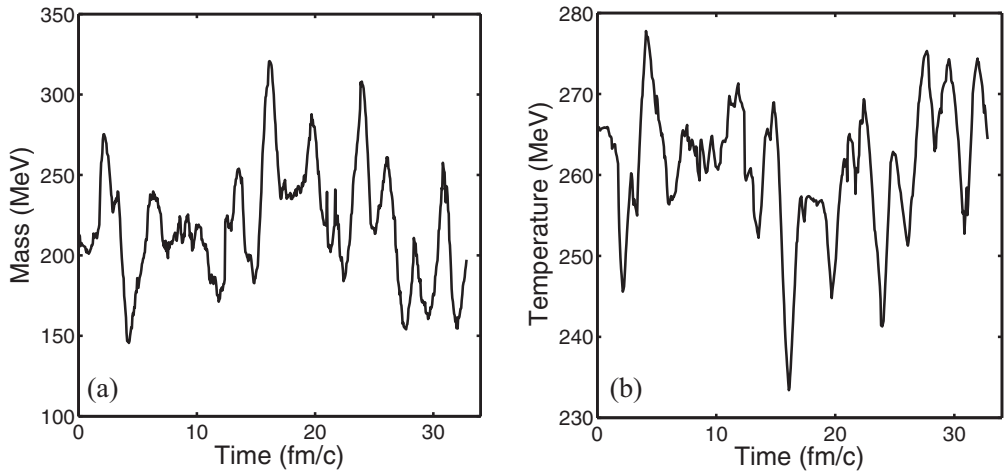


FIG. 15. Evolution of (a) the mean mass and (b) the mean temperature of the quarks, according to time.

in a volume equal to $8\,\mathrm{fm}^3$ correspond to a baryonic density close to $3\rho_0$. Moreover, the average momentum of each quark is chosen to be close to 780 MeV; it leads to a temperature slightly greater than 250 MeV. To simulate the behavior of an infinite system, the cube's walls are perfectly reflective for the trapped quarks. The inelastic reactions are not included in this test.

The results are presented in Figs. 15 to 19. First, one studies the evolution of some relevant physical quantities: the mean mass of the quarks, the mean temperature, and the mean Polyakov field $\Phi$ felt by these particles. Concerning this one, I observed in Ref. [45] that $\bar{\Phi} \approx \Phi$ whatever the temperature or the baryonic density. So, I only plot $\Phi$ in the graphs. The studied quantities present fluctuations according to time. More precisely, the mass oscillates around an average value close to 220 MeV. The average temperature is near 260 MeV, as expected. Furthermore, the variations of the masses and the ones of the temperature seem to be reversed. This aspect is explained by Fig. 2: For the observed temperatures, the mass of a light quark $q$ decreases almost linearly when the temperature is growing. Concerning $\Phi$, it is often above 0.5. *Stricto sensu*, the "deconfined" regime corresponds to $\Phi \to 1$. However, because of the effective potential Eq. (6), such a value is only reached at infinite temperature. In practice, it was observed [45,91] that $\Phi \approx 0.8$ at high temperatures, i.e., $T \approx 400\,\mathrm{MeV}$. Also, $T_0 \approx 270\,\mathrm{MeV}$, i.e., the critical deconfinement temperature in a pure gauge theory [83] (Table II). As a consequence, the $T$ and $\Phi$ found in Figs. 15 and 16 suggest that we are close to the "deconfinement transition." Therefore, this simulation corresponds to the description of a rather hot system. It may be associated with the conditions for which the hadronization is expected to occur.

In Fig. 16(b), I plot the evolution of the number of collisions according to time. As with the previous graphs, the results seem to oscillate around an average value. Concerning numerical aspects, a deviation of the values would have been the sign of a possible anomaly in the algorithms, or a badly chosen iteration time. In this test and in the following ones, I consider an iteration time $\Delta t = 5 \times 10^{-2}\,\mathrm{fm}/c$, in agreement with the reasoning of Ref. [80]. Concerning physical aspects, the found collision rate is consistent with the one observed in this reference, in close conditions.

Moreover, the fact that the values do not deviate is coherent for an isolated and closed system. It suggests that one describes

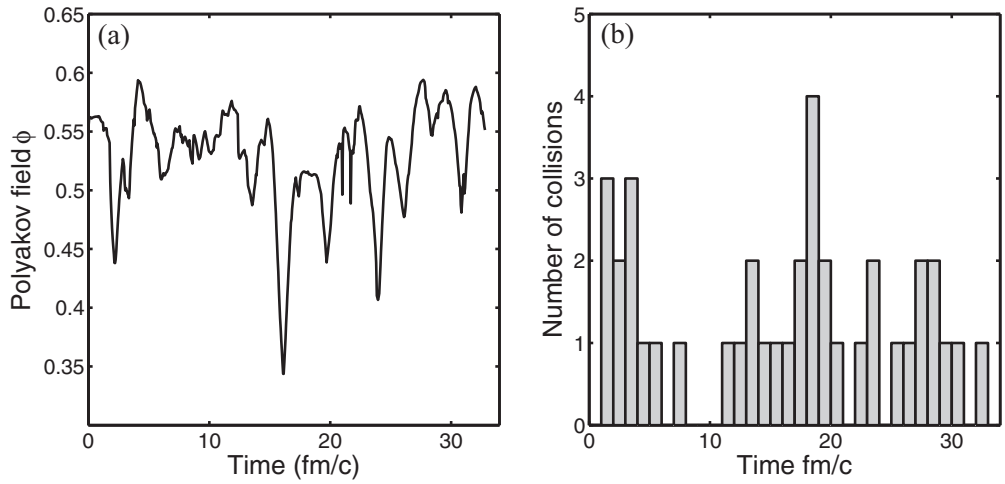


FIG. 16. Evolution of the (a) mean Polyakov field and (b) number of collisions, according to time.

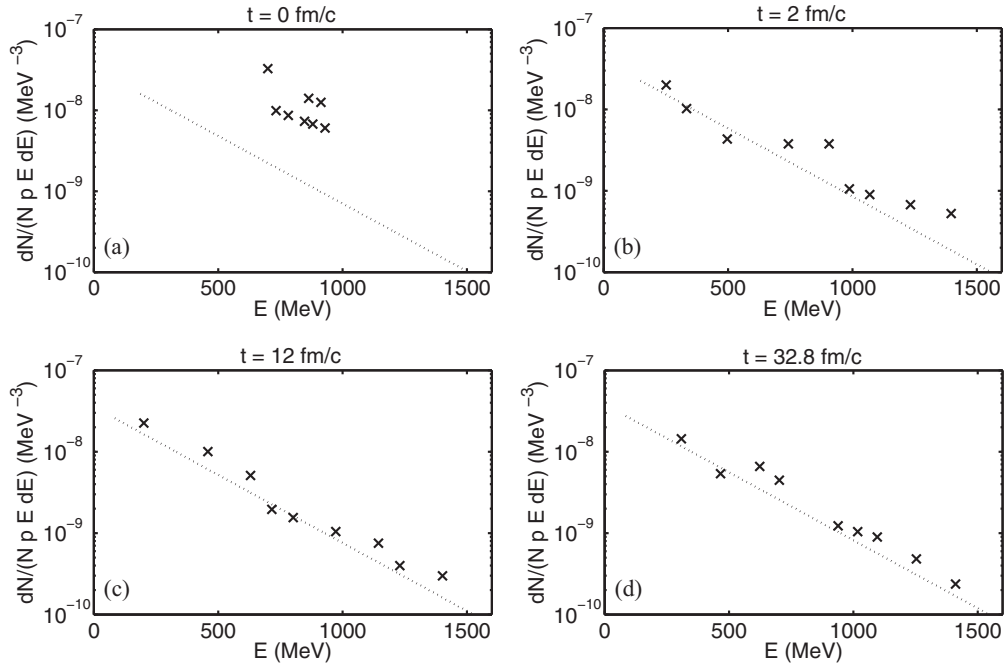


FIG. 17. Energy distribution of the quarks for several times: (a) in the beginning, (b) at $t = 2\,\mathrm{fm}/c$, (c) at $t = 12\,\mathrm{fm}/c$, and (d) in the end of the simulation. In the four graphs, the dashed line corresponds to the analytical distribution plotted for a temperature $T = 260\,\mathrm{MeV}$. This line starts for $E = m$.

a system at equilibrium. To validate this affirmation, I propose to study whether the system reaches kinetic equilibrium. I consider the Maxwell-Jüttner distribution $f_{MJ}$ [114,115]. For one relativistic particle of mass $m$, its distribution according to its energy $E$ is written, at a temperature $T$, as

$$f_{MJ}(E) = \frac{p\ E}{m^2\ T\ K_2(m/T)}\ \exp(-E/T), \qquad (31)$$

in which $p$ is the modulus of the momentum and $K_2$ is the modified Bessel function of the second kind. Therefore, at the kinetic equilibrium, the distribution $dN/(N\ p\ E\ dE)$ of $N$ identical particles should correspond to $[m^2\ T\ K_2(m/T)]^{-1}\ \exp(-E/T)$; thus, it should be proportional to $\exp(-E/T)$. As a consequence, with a logarithmic scale, this distribution should have a linear behavior according to $E$, whose slope depends on $T$. This method can be compared to the energy spectra visible in Refs. [67,116]. In addition, in the ultrarelativistic limit, $T \gg m$, $p \gg m$, so that $p \approx E$, $K_2(m/T) \sim 2\ (T/m)^2$, and the distribution becomes

$$\frac{dN}{N\ p\ E\ dE} \equiv \frac{dN}{N\ E^2\ dE} = \frac{1}{2T^3}\ \exp(-E/T). \qquad (32)$$

In other words, one finds the Boltzmann statistics for ultrarelativistic particles and one recovers the method evoked in Ref. [102] for box calculations.

The results are gathered in Fig. 17. The initial conditions are out of equilibrium: The found distribution is present in a too-reduced energy range in Fig. 17(a), and it is largely

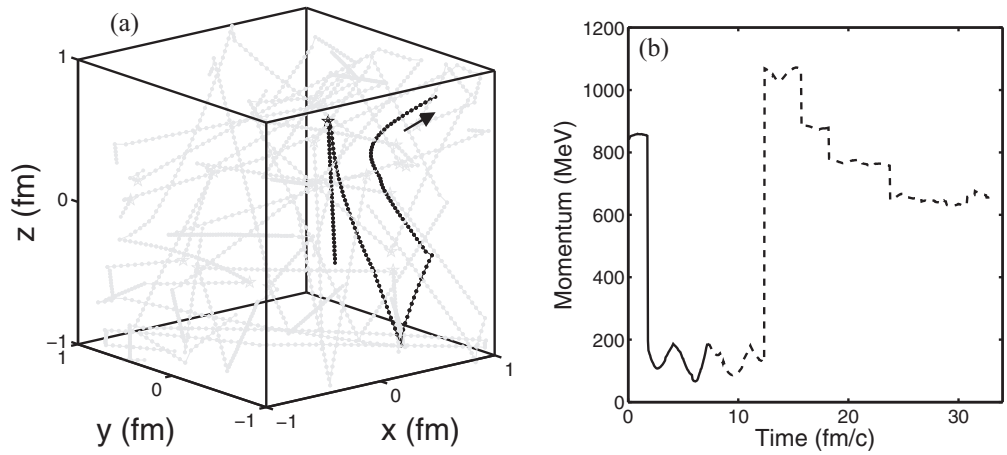


FIG. 18. (a) Simulation of 12 light quarks in a cube and (b) detail on the momentum of one of these quarks.

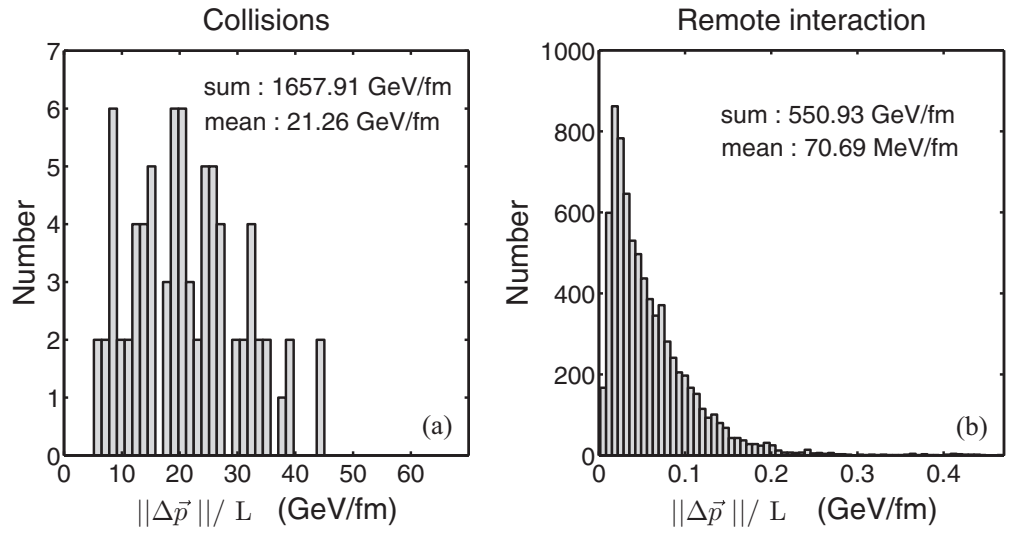


FIG. 19. Histograms of the change in momentum per unit path $\|\Delta\vec{p}\|/L$, (a) owing to the collisions and (b) owing to the remote interaction.

above the line representing the analytical distribution, Eq. (31). However, rapidly, except for some statistical fluctuations, the distributions become consistent with a kinetic equilibrium for a temperature $T = 260\,\text{MeV}$. This value corresponds to the average temperature found in the simulation. This equilibrium was reached rapidly thanks to the elastic collisions, which occurred in this simulation from $t \approx 1.2\,\text{fm}/c$. Indeed, they allowed the quarks to modify their momenta to obtain a distribution compatible with Eq. (31).

We turn our attention now to Fig. 18(a), in which the trajectories of the quarks are represented, in the first moments of the simulation, i.e., $0 \leqslant t \leqslant 7.2\,\text{fm}/c$. The collisions between the quarks are marked with stars. I highlighted the trajectory of one of the quarks. In Fig. 18(b), the momentum of this quark is plotted according to time. The solid line corresponds to the simulation times really represented in Fig. 18(a). The dotted line is associated with the ulterior moments of the simulation.

First, as a whole, the trajectories appear to be straight lines. It suggests that the remote interaction does not seem to intervene in this simulation in an important way. It can be explained by several reasons. Notably, the particles' momenta are higher than in Fig. 12: This short-range interaction does not have the time to really influence the quarks' trajectories. Then, another argument is the abundance of quarks in a reduced volume, leading to a rather homogeneous environment inside the box. Indeed, the remote interaction intervenes when the parameters felt by the particles present enough variations. Nevertheless, the underlined quark does not describe this behavior: Its trajectory is strongly curved, especially in the right part of the three-dimensional graph. This portion of the trajectory corresponds to simulation times between 3 and 7.2 $\text{fm}/c$. The quark's direction at this moment is indicated by the black arrow. The deviation of the quark's trajectory was induced by the other quarks present in its vicinity. In Fig. 18(b), for $3 < t < 7.2\,\text{fm}/c$, the quark's momentum is largely reduced compared to the mean momentum (780 MeV). It confirms the previous observations: The remote interaction between quarks can only act on slow quarks.

To analyze the importance of the remote interaction compared to the collisions quantitatively, I plot the histograms of the change in momentum per unit path $\|\Delta\vec{p}\|/L$ for the whole simulation. The quarks' rebounds on the walls are not included in these statistics. I obtain Fig. 19, in which the contribution of the collisions and the contribution of the remote interaction are separated. The collisions lead to rather important values of $\|\Delta\vec{p}\|/L$ between 5 and 45 GeV/fm, whereas the remote interaction involves greatly reduced ones. Indeed, in Fig. 19(b), values of $\|\Delta\vec{p}\|/L$ greater than 0.3 GeV/fm are very rare. However, one has 39 collisions in the simulation, i.e., 78 events in Fig. 19(a). It explains why this distribution is so irregular. In contrast, the histogram associated with the remote interaction concerns a total of 7794 events. The corresponding distribution is more regular; it exhibits an evolution comparable to an exponential decrease. Moreover, the mean contribution to the remote interaction (70.69 MeV/fm) is negligible compared to the contribution of the collisions (21.26 GeV/fm). However, if one performs the summation of the contributions for the two histograms, the sum associated with the remote interaction (550.93 GeV/fm) is only three times lower than the one of the collisions (1657.91 GeV/fm).

In the conditions of this simulation, i.e., involving high temperatures, these results lead us to conclude that the collisions seem to govern the quarks' dynamics. They dominate the effects of the remote interaction. The influence of this one appears to be rather limited, but cannot be totally neglected. Indeed, even if high temperatures involve rapid quarks, slow quarks can also be found in the distribution at kinetic equilibrium. The quark studied in Fig. 18(a) is an example and cannot be considered as an exception. However, these results cannot make it possible to predict the influence of the remote interaction in complete simulations, notably on the hadronization process.

TABLE VI. Initial composition of the system.

| Particle | $u$ | $\bar{u}$ | $d$ | $\bar{d}$ |
|---|---|---|---|---|
| No. | 30 | 20 | 36 | 25 |

## V. ANALYSIS OF FIRST SIMULATIONS

### A. Comparison between NJL and PNJL results

One considers a spherical system initially composed of light quarks and antiquarks [Table VI and Fig. 20(a)]. The matter dominates the antimatter: The quark/antiquark ratio is close to 1.5. The distribution of the momenta is inhomogeneous [Fig. 20(b)]. High momenta are synonymous with high temperatures. Thus, one objective is to obtain a layer structure, with a hot core and colder external layers, comparable to the profile observed in Ref. [80]. Figure 23(a) shows that the obtained temperature profiles are in agreement with this description. However, in Ref. [80], for a fixed radius $r$, the momentum distribution corresponds to one unique $p$ value. In the description, I propose an evolution of this distribution by including a dispersion of the momenta. For each layer, the purpose is to be consistent with a thermal distribution. More precisely, in the case of massive particles, I consider the Maxwell-Jüttner distribution [114], introduced in Sec. IV B. It leads to a distribution as $f_{MJ}(\|\vec{p}\|) \propto p^2 \exp(-E/T)$, thus to an increase in the dispersion when the temperature goes up. As observed in Fig. 23(a), the variations of the temperature appear to be rather slow according to the radius $r$, in agreement with the notion of local equilibrium evoked in Sec. III A. However, the statistics are small near the center of the sphere. They lead to the imperfect sampling visible in Fig. 20(b), notably when $r < 1$ fm.

Then one proceeds to NJL and PNJL simulations, using each time exactly these initial conditions. The system is open, i.e., not confined in a box as in Sec. IV B. The results are presented in Figs. 21 and 22 and in Table VII. The evolution of the number of quarks/antiquarks according to time is shown in Fig. 21, whereas Fig. 22 is devoted to mesons. These data correspond to two simulations, but I checked that other tests gave similar results. More precisely, in the collision algorithm described in Sec. III C, one stage of the procedure uses stochastic considerations. It leads to statistical fluctuations. However, the variations concern few particles in these results, typically less than 5 quarks/mesons. Moreover, being aware of the relative fragility of composite antiparticles $\bar{D}$ and $\bar{B}$ in the matter, these ones were not included in these simulations.

The results confirm the predictions formulated in Sec. IV B: The quark remote interaction acts in a rather negligible way in this simulation. As visible in Fig. 20, the quarks located in the most external layers seem to be slow enough to undergo this interaction. It leads to some modifications of the trajectories of these quarks. However, the cross sections can be rather high, especially with $q + \bar{q} \to M + M$. Therefore, the deviations of the trajectories are not strong enough to interfere with the collisions. Furthermore, the quarks coming from the core or from the hot layers are too rapid to undergo the remote interaction. As a consequence, rectilinear trajectories were found for them.

Concerning the quarks/antiquarks and mesons, their populations do not seem to vary after $t > 20\,\mathrm{fm}/c$, with the (P)NJL models. The simulations ended at $t = 30\,\mathrm{fm}/c$: This simulation time corresponds to the "final state" of the system. Table VII indicates its composition at this time. The production of diquarks and baryons is strongly reduced. As a consequence, the evolution of the system can be studied via Figs. 21 and 22. As a whole, the production of the mesons is optimal in the first moments of the simulation. It induces a diminution of the quarks/antiquarks' population in a symmetrical way. This strong mesonization is explained by the high concentration of quarks and antiquarks, leading to an important collision rate. The attractive quark interaction does not intervene in a notable way. Therefore, the system extends spatially. It leads to a dilution of the particles and thus to a diminution of the collision rate. When the expansion becomes too strong, the particles no longer interact. It explains the stagnation when $t > 20\,\mathrm{fm}/c$.

An important aspect of the results concerns the found differences between the NJL and the PNJL models. The mesons' production is more rapid and more efficient in the PNJL description than in a pure NJL one. Indeed, the number of

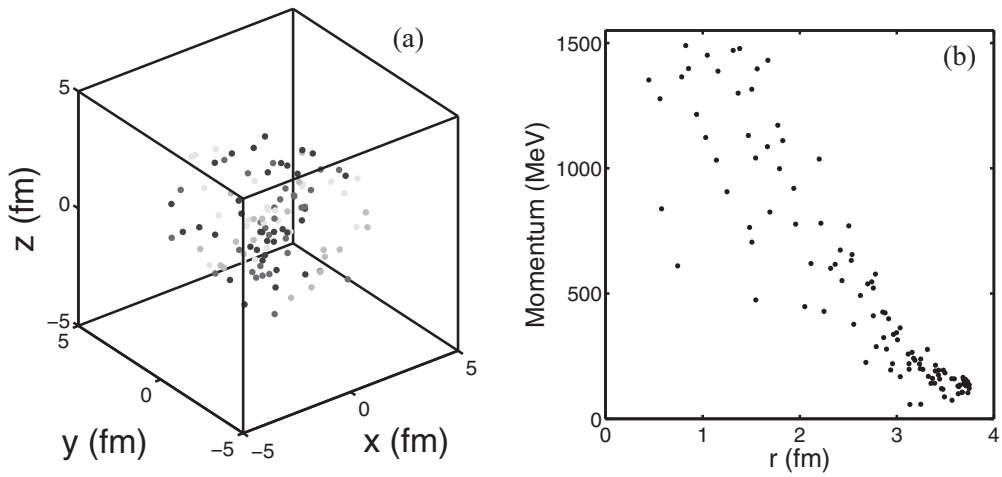


FIG. 20. (a) Initial positions and (b) momenta of the quarks involved in the simulations.

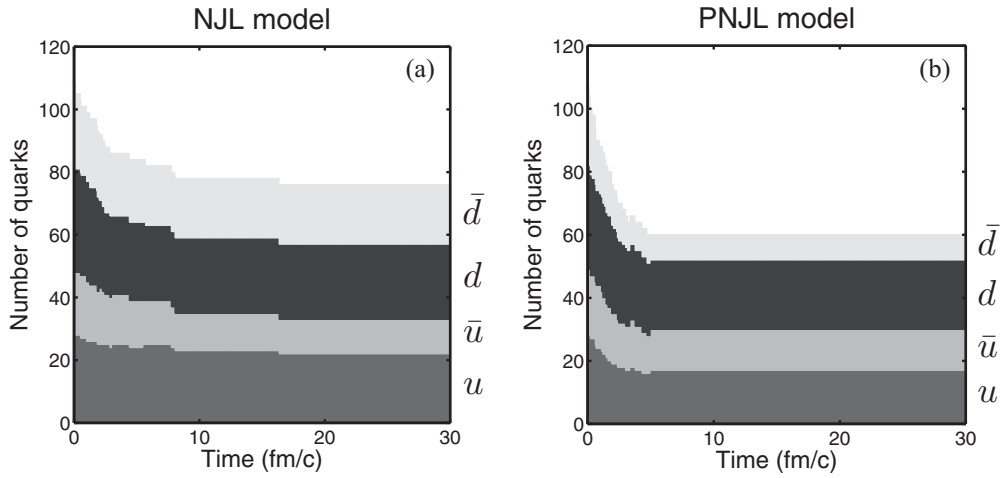


FIG. 21. Evolution of the quarks' population according to time, with (a) NJL and (b) PNJL.

mesons stagnates with PNJL when $t > 5\,\mathrm{fm}/c$, versus $15\,\mathrm{fm}/c$ with NJL. Furthermore, the production of mesons is equal to 50 with PNJL and 33 with NJL. Such a difference is explainable thanks to Fig. 23. This one shows the initial temperatures felt by the quarks/antiquarks and their initial masses. Even if the initial positions and momenta were strictly equal in the (P)NJL simulations (Fig. 20), the calculations of the quark masses, Eqs. (1) and (12), and the temperatures Eq. (27) do not give the same results in the two models. The initial temperatures are slightly lower in the PNJL model than in the NJL one. In contrast, the masses are stronger with PNJL than with NJL, notably in the core, i.e., $r < 1.5\,\mathrm{fm}$. This mass difference could intervene in the quarks' dynamics, e.g., in the first equation of Eq. (29) via the energy. However, the concerned quarks are highly relativistic, so the masses are negligible in front of the momenta. As a consequence, the mass difference between NJL and PNJL does not lead to the observed discordances in Figs. 21 and 22.

However, as explained in Ref. [94], the optimal temperature (at null density) of the mesonization process, via $u + \bar{u} \to \pi^+ + \pi^-$, is close to 230 MeV for the NJL model [32,94] and 280 MeV for the PNJL one (Fig. 6). These results can be extrapolated to the other mesonization reactions of this kind, involving light quarks and pions. In addition, $u + \bar{u} \to u + \bar{u}$ is optimal for a temperature 20 MeV above the ones found for the mesonization reactions in the (P)NJL models. Concerning the NJL simulation (Fig. 23), a significant part of the system is initially too hot to undergo the mesonization. In the core, the quark/antiquark elastic reactions dominate the other reactions, at least in the first instants of the expansion. It leads to a reduced production of mesons, which mainly occurred in the external layers in the beginning of the simulation. In contrast, in the PNJL simulation, the initial temperatures are below 280 MeV in all the system. Even if the mesonization is not optimal for $T < 280\,\mathrm{MeV}$, the cross sections stay rather strong, especially near the kinematic threshold [54,94]. As a consequence, in the PNJL simulation, the mesonization can start in all the system, since the beginning of the simulation. It leads to the observed production of mesons.

However, the two models do not reach a complete hadronization in these simulations. 68% of the quarks/antiquarks are still free in the end of the simulation

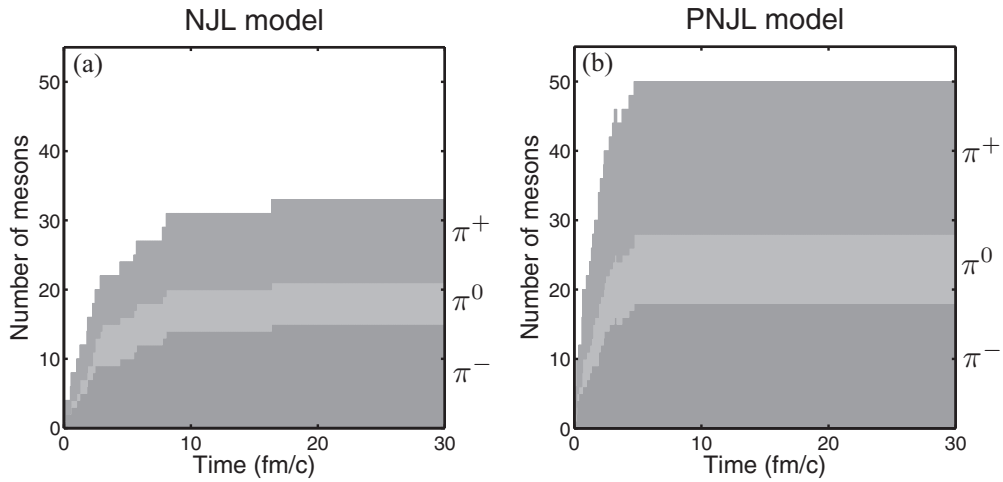


FIG. 22. Mesons' production according to time, with (a) NJL and (b) PNJL.

TABLE VII. Composition of the system at $t = 30\,\mathrm{fm}/c$.

| Particle | Quark | Meson | Diquark | Baryon |
|---|---|---|---|---|
| NJL | 76 | 33 | 1 | 1 |
| PNJL | 60 | 50 | 0 | 1 |

with the NJL model, and 54% are still free with PNJL. It is conceivable to improve these results, notably at the level of the initial system composition, geometry, momenta, etc. However, the (P)NJL models alone do not seem to be able to allow a full hadronization of such open systems. A possible explanation of this phenomenon can be related to the relative weakness of the cross sections associated with the baryonization processes, notably compared to the ones found for $q + \bar{q} \to M + M$ [94]. Thus, it seems realistic to reach high hadronization yields with systems equitably composed of quarks and antiquarks. In these systems, a total hadronization is possible exclusively via the mesonization, i.e., without the baryonization as in Ref. [80]. Moreover, we saw the possibility to model a short-range interaction between quarks. However, this one proved to be too limited in this configuration. As a consequence, these results show the necessity of a long-range interaction, as the one modeled by QCD. Its purpose is to limit the velocity of the system expansion, at least for the quarks/antiquarks, to allow the quarks to combine into diquarks and then into baryons.

### B. A solution to obtain a complete hadronization

To solve the problem evoked in Sec. V A, several options are available. The objective is to find a mechanism that can model the long-range interaction. It may lead to modifications of the (P)NJL models. However, in this paper, I propose to add a sphere that will confine the quark-antiquark system described in Fig. 20. Thus, it mimics the behavior of the long-range springlike force. This sphere acts as the box in Sec. IV B; i.e., its wall is perfectly reflective for the quarks, antiquarks, and diquarks confined in this structure. These colored objects form the "QGP phase" inside the sphere. In contrast, the noncolored ones, i.e., mesons and baryons, can leave it freely. This confining sphere can be seen as a bag model, with a null potential inside the sphere and infinite potential outside for the colored particles. Its purpose is to avoid that these ones escape. The populations of quarks, antiquarks, and diquarks decrease during their hadronization. To take this aspect into account, the radius of the sphere is periodically updated. More precisely, its volume is proportional to the total number of quarks/antiquarks free or combined into diquarks. So the sphere shrinks progressively during the hadronization, until its disappearance when all the colored objects are combined into hadrons. This evolution is, e.g., visible in Fig. 33. The system is expected to keep a spherical symmetry during the simulation. Thus, the center of the sphere coincides with the center of the whole system.

I perform a PNJL simulation with this confining sphere. The populations of each type of particles are studied in Figs. 24 to 26. The inclusion of the sphere leads to a complete hadronization: The number of quarks/antiquarks converges towards zero, and there is no diquark in the end the simulation. The hadronization is fully completed at $t \approx 86.6\,\mathrm{fm}/c$. This time is longer than the one expected in Refs. [70,80]. However, the evolution of the number of quarks/antiquarks and mesons observed in Figs. 24 and 25 recalls the one predicted in Ref. [70]. More precisely, the mesons' production is strong in the first moments of the simulation, until $t \approx 8\,\mathrm{fm}/c$, via $q + \bar{q} \to M + M$. Then, the production begins to be less rapid, until $t \approx 25\,\mathrm{fm}/c$. After that, the variations of the number of mesons are slow, but rather regular. However, in this last phase, the mesons are produced by reactions as $q + D \to M + B$, and not by $q + \bar{q} \to M + M$. Even if the sphere avoids that the quarks/antiquarks leave the QGP phase (inside the sphere), the collision rate tends to decrease according to time. As observed in Fig. 35 with another simulation, this diminution cannot be associated with a modification of the conditions in the QGP phase. Indeed, an indirect effect of the sphere is to stabilize its temperature and its densities rapidly, and the update of its radius makes it possible to keep these parameters rather constant. More precisely, the temperature of the QGP phase is close to 200 MeV during almost all the simulation described in this Sec. V B. In fact, the reason for the diminution is related to kinematic considerations. With reactions as

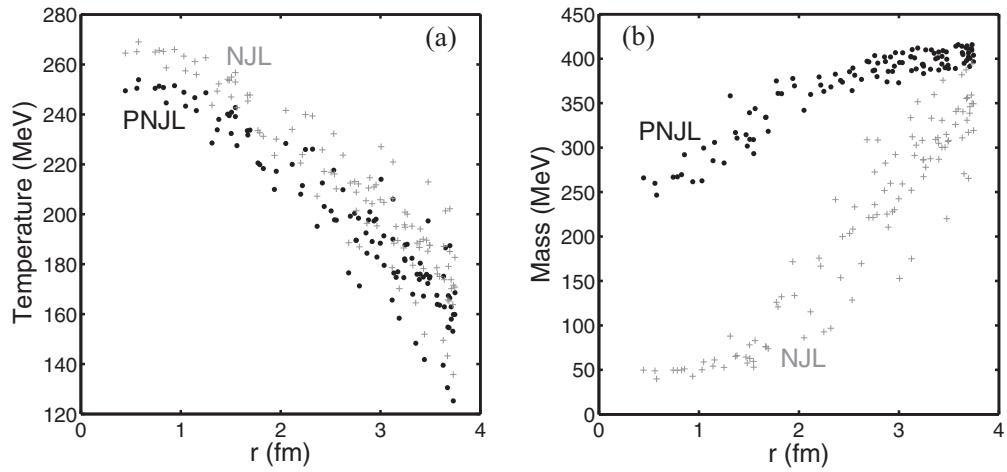


FIG. 23. (a) Initial temperatures and (b) initial masses.

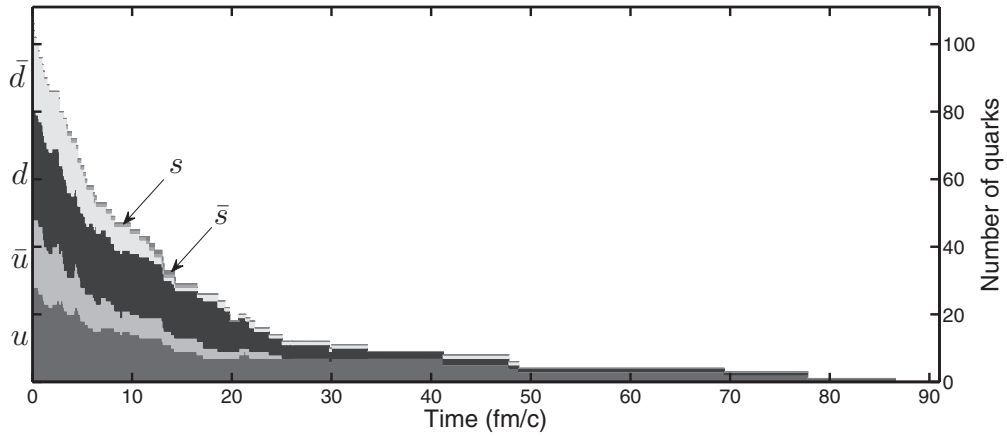


FIG. 24. Evolution of the number of quarks/antiquarks according to time.

$q + \bar{q} \rightarrow M + M$, the cross sections reach maximum values near the kinematic threshold. Therefore, the probability of creating mesons is optimal if the momenta of the incoming quark/antiquark are weak in the center-of-reference frame of these two particles (Appendix B). In the beginning of the simulation, the great number of $q/\bar{q}$ makes highly probable the satisfaction of this condition. However, as soon as the number of quarks/antiquarks decreases, the probability also decreases. In addition, rapid $q/\bar{q}$ are not favored by this kinematic condition. They may stay in the QGP phase for a long time before their hadronization. However, elastic reactions make it possible to decrease their momenta. Therefore, they lead these particles to react more easily via inelastic processes.

Moreover, rapid quarks/antiquarks can also be good candidates to react via reactions involving strange matter, as, e.g., $u + \bar{u} \rightarrow s + \bar{s}$, $u + \bar{d} \rightarrow K^+ + \bar{K}^0$, or $u + \bar{u} \rightarrow K^- + K^+$. These reactions have modest cross sections and their kinematic thresholds are higher than the ones of reactions exclusively involving light particles. However, they cannot be neglected for moderate $\sqrt{s}$ [32,48]. The inclusion of the sphere avoids that the rapid quarks/antiquarks quit the system. In the same time, this trick makes it possible to increase the number of collisions during the simulation. As a consequence, Fig. 24 shows that strange quarks and antiquarks are produced. Furthermore, a production of kaons is observed (Fig. 25 and Table VIII). As expected, this production is weak compared to the one of the pions. In the same way, a $\Sigma^+$ baryon is formed (Fig. 26).

Concerning the baryons, their production starts later in this simulation, i.e., after 16 fm/$c$. We do not take into account the nucleons formed before 10 fm/$c$, because they were destroyed rapidly by inelastic processes. These observations confirm the scenario formulated in Ref. [94] that imagined that the mesonization would occur before the baryonization to "consume" enough antiquarks and so to block processes that can destroy baryons, as $\bar{q} + B \rightarrow q + q$ and $\bar{q} + B \rightarrow M + D$. Moreover, no free antiquark (not combined into mesons) is found in the system first for $t \approx 33.6$ fm/$c$ and then definitively from $t \approx 48.8$ fm/$c$. Thus, the mesonization is completed earlier than the baryonization.

### C. Study of the kinetic and chemical equilibrium

To conclude this section, I recall that the initial temperature is not uniform [Fig. 23(a)] because of the initial conditions. Clearly, the system is initially out of an overall kinetic equilibrium. The question is now to investigate if the equilibrium is reached during the performed simulations, with or without the confining sphere. As in Sec. IV B, I use the distribution $dN/(N\ p\ E\ dE)$ to answer this question. Figure 27 gathers the results related to the simulation described in Sec. V B,

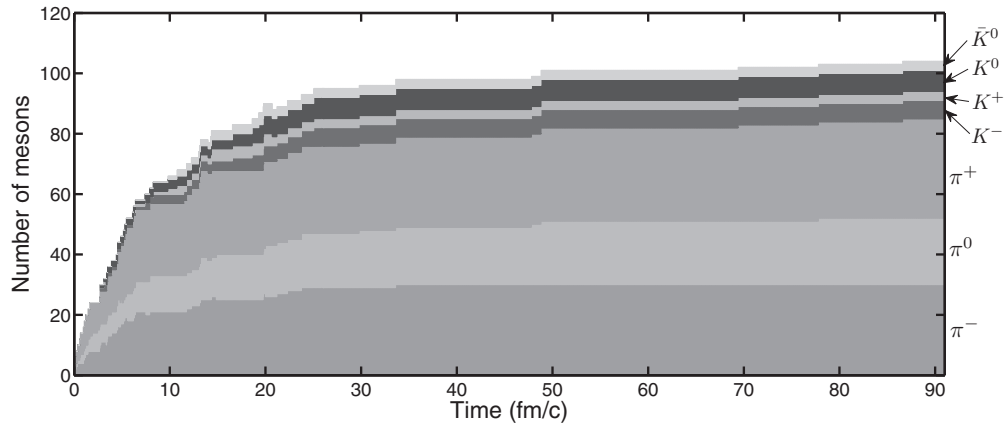


FIG. 25. Production of mesons according to time.

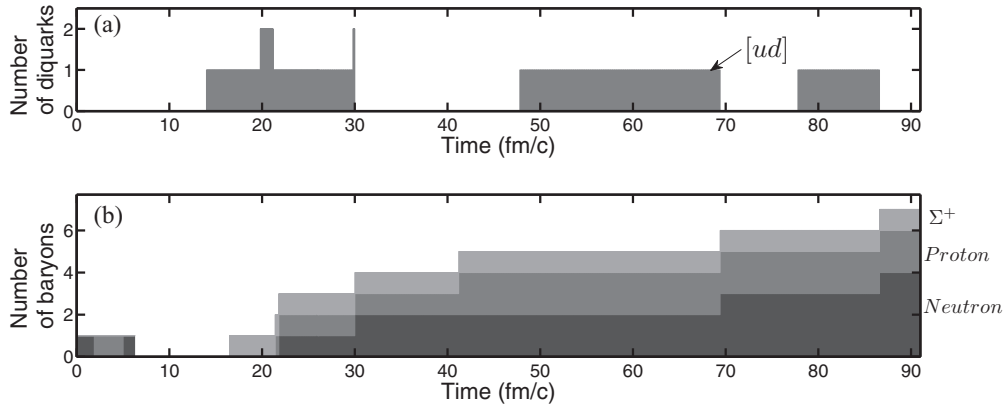


FIG. 26. Number of (a) diquarks and (b) baryons, according to time.

i.e., with the sphere, whereas Fig. 28 concerns the boxless NJL/PNJL simulations of Sec. V A.

First, Fig. 27(a) confirms that the initial distribution of the quarks/antiquarks does not correspond to an overall kinetic equilibrium. However, this one seems to be reached when $t \approx 10\,\mathrm{fm}/c$. Indeed, except some imperfections, the found distribution is consistent with the analytical one plotted for a temperature $T = 200\,\mathrm{MeV}$. As mentioned in Sec. V B, the QGP phase, located inside the sphere, stabilizes rapidly at this temperature until its disappearance. Also, the maximal energy of the $q/\bar{q}$ evolves from 1.5 GeV towards approximately 2 GeV. If one integrates Eq. (31) according to the energy from $m$ until 2 GeV, one finds $\approx$0.996, i.e., very close to the ideal value 1. This result confirms my conclusion.

The study that motivated Fig. 27(a) is similar to the ones described in Fig. 17 or in Ref. [102], which consider simulations in a box. However, the kinetic equilibrium can also be studied for the hadrons present in the system at the end of the simulation. Indeed, as soon as they are produced in the sphere, they leave it, and then their momenta will no longer be modified. In fact, the interactions between the hadrons outside of the sphere are negligible. As a consequence, the distributions of the hadrons plotted in Fig. 27(b) stay consistent with the temperature that most of them felt when they still were in the sphere, i.e., 200 MeV. This reasoning supposes low variations of the masses between the temperature in the sphere and the one measured when the distribution is plotted ($T$ close to zero, because of the dilution). This constraint is verified with these hadrons. Moreover, as in Refs. [67,116], in which similar energy spectra are established, the temperature is identical for each studied species. It reveals that the overall kinetic equilibrium is reached in this simulation. Nevertheless, differences compared to the analytical distributions are found at high energies. They are explainable by statistical fluctuations: They concern a reduced number of particles.

TABLE VIII. Final composition of the system.

| Particle | $\pi^-$ | $\pi^0$ | $\pi^+$ | $K^-$ | $K^+$ | $K^0$ | $\bar{K}^0$ | Neutron | Proton | $\Sigma^+$ |
|---|---|---|---|---|---|---|---|---|---|---|
| No. | 30 | 22 | 33 | 6 | 3 | 7 | 3 | 4 | 2 | 1 |

Also, I recall that mesons are produced in the beginning of the simulation, i.e., when the temperature is not uniform. However, for these ones, I underline the contribution of the elastic processes $M + M \to M + M$, $q + M \to q + M$, and $\bar{q} + M \to \bar{q} + M$, which drive these mesons towards the kinetic equilibrium.

The reasoning done for the hadrons is also applicable to the boxless simulations studied in Sec. V A (Fig. 28). In this way, I represent the distributions of the pions, in the NJL and PNJL simulations, respectively, in Figs. 28(a) and 28(b). Also, in Figs. 28(c) and 28(d), I consider the distributions of the quarks/antiquarks in the same simulations. In fact, even if the system is initially out of the overall equilibrium, the expansion of the central zone towards the cold layers allows the particles to mix. Therefore, the temperature becomes more homogeneous: It is close to 200 MeV when a part of the pions is produced. The other part concerns the pions produced early, before the mix. They were evoked in Sec. V A to explain the difference between the NJL and PNJL results. As in the previous paragraph, their thermalization is explainable by the elastic processes that occur at this moment. More precisely, one also quotes the pion-pion scattering and the elastic reactions involving a pion and a quark/antiquark. As a consequence, the pion distributions are consistent with the analytical distribution plotted for $T = 200\,\mathrm{MeV}$. Thus, these distributions indicate that the pions are close to kinetic equilibrium, notably with the PNJL model. However, they are less regular than the one of Fig. 27(b).

Moreover, the distributions of the quarks/antiquarks show that these ones also evolve towards an equilibration. As in Secs. IV B and V B, the evolution of the $q/\bar{q}$ spectra is attributable to the elastic collisions. When these ones cease because of the dilution, the momenta of the quarks/antiquarks are fixed. As a consequence, the found results correspond to a "snapshot" of the $q/\bar{q}$ phase just before the kinetic freeze-out. According to the graphs, their temperature is comparable to 200 MeV at this moment. Obviously, the variations of the quark masses constitute a limitation of this reasoning, notably with NJL (Fig. 2). Moreover, the deviations observed for $E \approx 1$ GeV in Figs. 28(c) and 28(d) lead us to conclude that the kinetic equilibrium is not complete for the $q/\bar{q}$ phase. Because of the absence of the sphere, an explanation is a lack of elastic

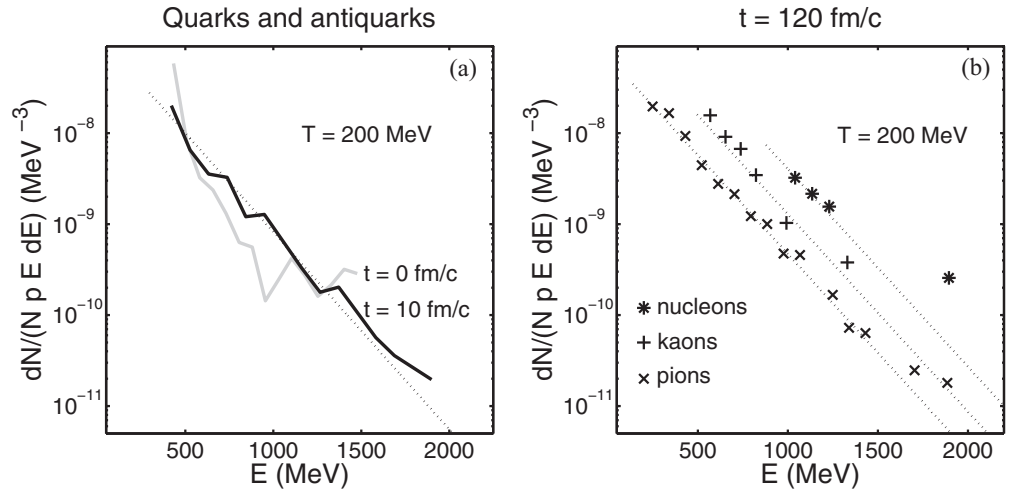


FIG. 27. (a) Distributions of the quarks/antiquarks and (b) distributions of the hadrons in the end of the simulation described in Sec. V B. The dashed lines mark the analytical distributions of each particle type, for a temperature $T = 200$ MeV. Each line starts at $E = m$.

collisions in these (P)NJL simulations. As a consequence, the comparison of Figs. 27 and 28 makes it possible to see that the system can evolve towards kinetic equilibrium even without the sphere. However, this evolution is more efficient thanks to this one, notably for the quarks: The sphere allows them to reach the equilibrium.

Concerning the notion of chemical equilibrium, there is a method that consists of comparing, for each species, the found number $N$ of particles with the theoretical one $N_{\text{eq}}$ at equilibrium, estimated by a statistical calculation. For example, Refs. [102,103] consider the fugacity $\lambda = N/N_{\text{eq}}$. Also, in Refs. [67,116], the yields for each hadron type are studied. It enables a comparison with theoretical estimations, performed in an ideal hadron gas modeling. For a system considered as infinite, $N_{\text{eq}}$ is evaluated by

$$N_{\text{eq}} = \frac{g\,V}{2\pi^2}\int_0^\infty p^2\, f_{F,B}\,(p)\,dp, \tag{33}$$

where $g$ is a degeneracy factor and $V$ is the volume of the box in which the simulation is performed. $f_F$ and $f_B$ are, respectively, the Fermi-Dirac and Bose-Einstein statistics. In the case of ultrarelativistic particles, Eq. (33) can be simplified and calculated analytically, which leads to the

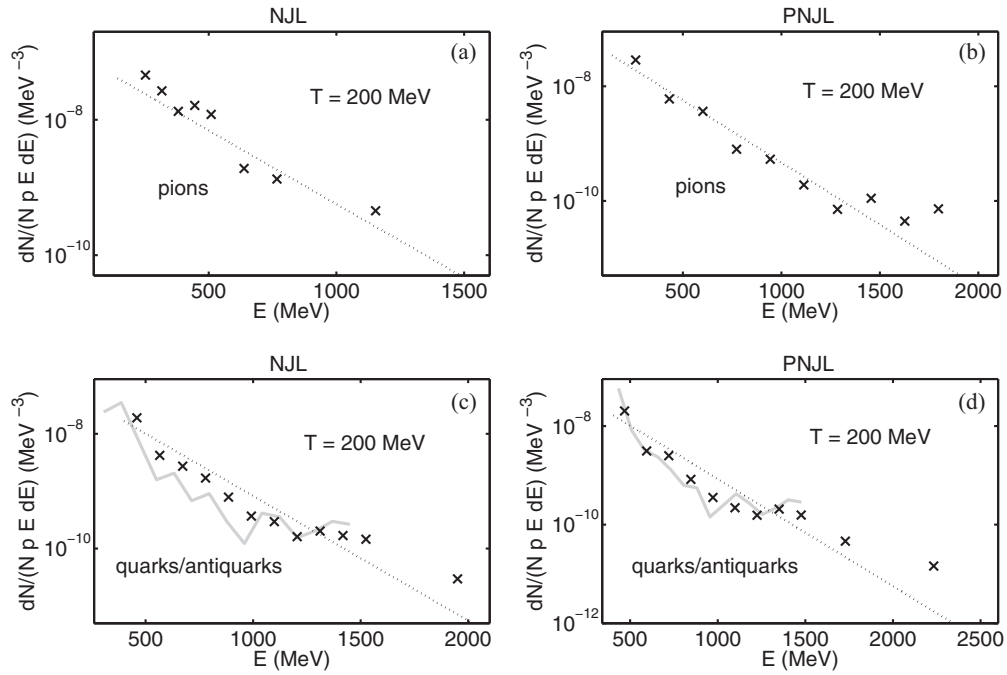


FIG. 28. Distributions of the pions, in the (a) NJL and (b) PNJL simulations performed in Sec. V A and distributions of the quarks/antiquarks in the same (c) NJL and (d) PNJL simulations. The gray curve is the initial $q/\bar{q}$ distribution. The dashed lines are the analytical distributions plotted for $T = 200$ MeV.

TABLE IX. Number $N$ of hadrons found in Sec. V B and theoretical estimations $N_{eq}$.

| Particle | Pion | Kaon | Nucleon | Σ |
|---|---|---|---|---|
| $N$ | 85 | 19 | 6 | 1 |
| $N_{eq}$ | 74 | 38 | 8 | 4 |
| $N_{eq}$ with Eq. (34) | 53 | 29 | 7 | 3 |

relation $N_{eq} = g\ T^3\ V/\pi^2$ mentioned in Ref. [102]. However, in the framework of my simulations, this simplification cannot be applied. Indeed, we are not in this regime, as seen in Sec. IV B, maybe except for the pions.

One assimilates the simulation described in Sec. V B to a box simulation, with $T \approx 200$ MeV. It constitutes an approximation performed to calculate $N_{eq}$. The initial radius of the sphere is $R = 3.8$ fm, which makes it possible to estimate $V$. To take into account the finite size of this system, I follow the reasoning of Ref. [117]; i.e., I multiply the integrand in Eq. (33) by the correction factor

$$F_{corr} = 1 - \frac{3\pi}{4p\ R} + \frac{1}{(p\ R)^2}. \tag{34}$$

Table IX recalls the results found in Sec. V B and presents the data found with Eq. (33), using or not Eq. (34). For each species, $N$ and $N_{eq}$ appear to be comparable. However, the number of pions exceeds the ones found by the statistical calculations. In contrast, the number of kaons seems to be too reduced: One has $\lambda \approx 0.50$ with Eq. (33) and $\lambda \approx 0.66$ if one uses Eq. (34). According to these calculations, the strangeness production is not strong enough in this simulation. Indeed, even if the formation of strange matter starting from $q/\bar{q}$ is possible, it remains weak compared to reactions exclusively involving nonstrange particles. This strangeness deficit is discussed in Sec. VI. Concerning the number of baryons, the values found in the simulation are rather close to the theoretical ones, notably for the nucleons. However, these small statistics cannot allow these results to be significant.

TABLE X. Initial composition of the system.

| Particle | $u$ | $\bar{u}$ | $d$ | $\bar{d}$ |
|---|---|---|---|---|
| No. | 86 | 43 | 100 | 50 |

## VI. COMPLETE STUDY OF A SIMULATION

The simulations performed in the previous section used a rather reduced number of particles. As a consequence, we cannot be sure that the modest diquark production (Fig. 26) can be considered as a general result. So, I proceed to a new PNJL simulation, involving 279 particles. The initial composition is presented in Table X. Compared to Table VI, the asymmetry between matter and antimatter is enhanced: One has two times more quarks than antiquarks. The initial positions and momenta of the particles are represented in Fig. 29. In the previous simulation, the initial radius was about 3.8 fm, versus 4.5 fm now. Moreover, the maximal momenta exceed 1500 MeV, i.e., more than for the ones described in Fig. 20.

These initial conditions lead to a hot and dense system (Figs. 30 and 31). First, the initial temperature in the core exceeds 300 MeV, i.e., more than the 280 MeV associated with an optimal mesonization. The temperature decreases progressively as the radius increases. In the most external layers, the values exceed 180 MeV. Moreover, the masses of the quarks/antiquarks are low in the core, but stay greater than their naked masses. Indeed, in the PNJL model, the naked values are reached for temperatures greater than or equal to 400 MeV (Fig. 2). However, the values of the Polyakov field $\Phi$ are close to 0.7 in the core. Thus, we can consider that the quarks/antiquarks are there in a "deconfined" regime. Moreover, the densities were not described in the previous simulations. However, here, they have strong values (Fig. 31). The profiles of the densities $\rho_u$ and $\rho_d$ are rather similar, even if the $\rho_d$ are slightly raised, because of the excess of $d$ quarks compared to $u$ ones. With the relation $\rho_B = 2/3\ \rho_q$ [21] seen

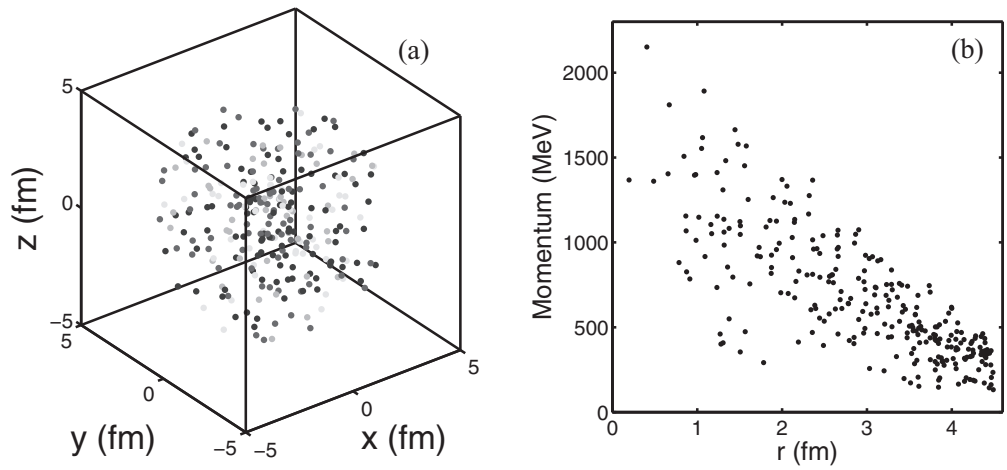


FIG. 29. (a) Initial positions and (b) initial momenta.

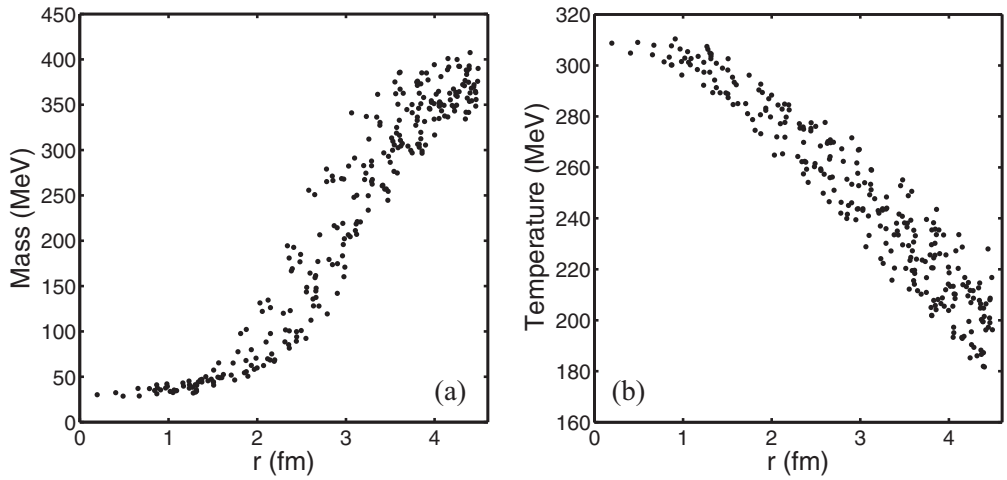


FIG. 30. (a) Initial masses and (b) initial temperatures.

in Sec. II A, one estimates that the baryonic density is close to $3\rho_0$ in the core.

The evolution of the particles' populations is represented in Fig. 32. Concerning the quarks/antiquarks and the mesons, their evolutions strongly recall the ones observed in Figs. 24 and 25. Roughly speaking, the population of quarks/antiquarks is decreasing exponentially. However, concerning the diquarks and the baryons, differences are observable compared to that seen in Fig. 26. Here a massive production of diquarks occurs in the first moments, until $t \approx 10\,\mathrm{fm}/c$. During $\approx 15\,\mathrm{fm}/c$, the number of diquarks stagnates and then decreases exponentially. About the baryons, their production really starts at 3.7 $\mathrm{fm}/c$. At first, the number of baryons is rather modest, until $t \approx 25\,\mathrm{fm}/c$. Then the production becomes stronger. This aspect is explained by the consumption of the diquarks to form the baryons. More precisely, the diquarks perfectly play the role of intermediate states. By their non-negligible production, they allow a more efficient creation of baryons, notably when $30 < t < 60\,\mathrm{fm}/c$. In this simulation, this behavior is explainable by the temperatures and densities obtained in some layers of the system, allowing reactions as $q + q \to M + D$. Indeed, it was seen in Fig. 7 [94] that $u + d \to [ud] + \pi^0$ has optimal cross sections for densities close to $2 - 3\rho_0$ and temperatures of about 200 MeV or more.

Figure 32 is completed by Table XI. This one describes the final composition, once the hadronization is complete, i.e., for $t = 133.4\,\mathrm{fm}/c$. As with Table VIII, the production of pions is strong. They constitute about 79% of the particles found in the end of the simulation. In addition, we observe the production of 26 nucleons. They represent slightly less than 10%. Moreover, the formation of strange particles also occurred. One managed to produce rare particles because one included more particles and because one reached higher temperatures than in the previous simulation. In fact, thanks to the conditions met in this simulation, $s,\bar{s}$ pairs have been produced by $q + \bar{q} \to s + \bar{s}$. They allowed the formation of a $[us]$ diquark. In the final state, we have $\eta$ mesons and the hyperons $\Sigma^-, \Sigma^+$, i.e., particles formed by reactions presenting very limited cross sections.

We turn our attention now to Fig. 33, which shows the evolution of the temperature according to the distance from the center of the system ($r$) and according to time. In this graph,

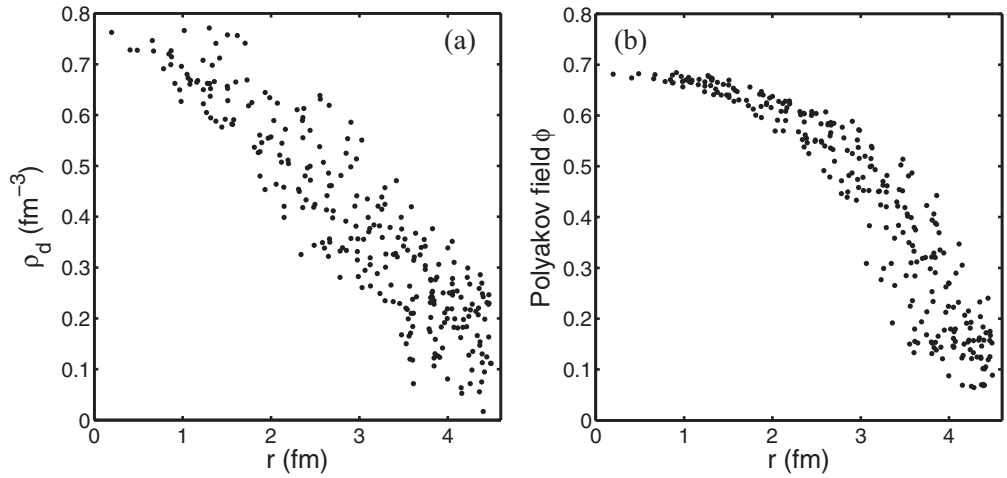


FIG. 31. (a) Initial $\rho_d$ density and (b) initial Polyakov field.

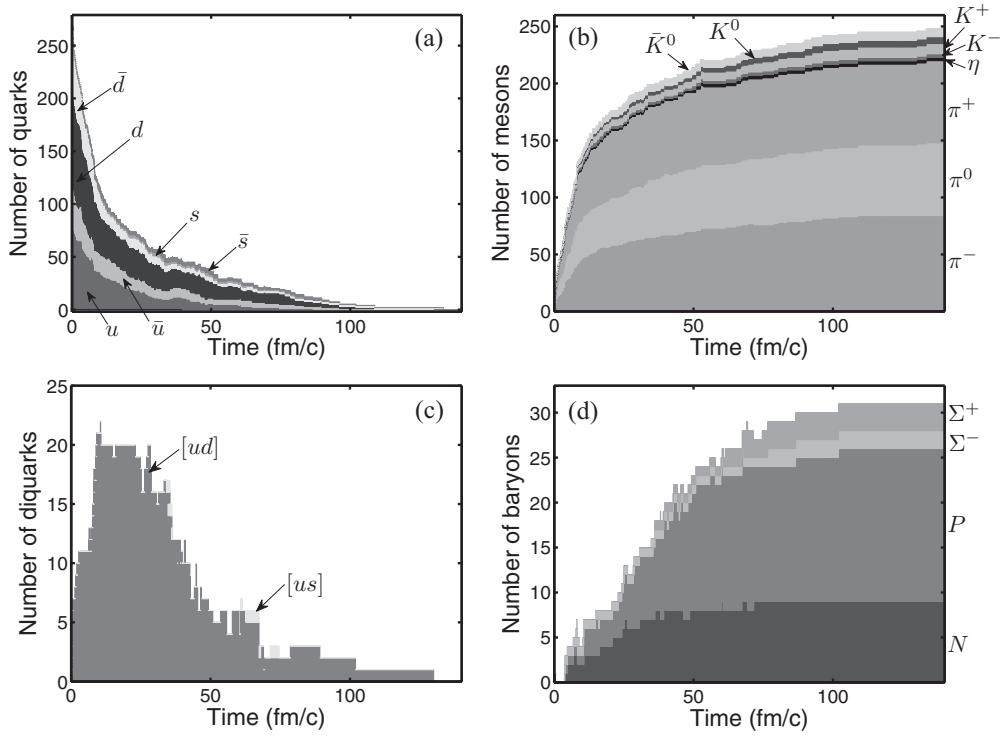


FIG. 32. Evolution of the particles' populations according to time. $P$ corresponds to protons, and $N$ corresponds to neutrons.

I also plotted the radius of the sphere. The zone to the left of this curve represents the phase formed by the quarks/antiquarks and the diquarks, i.e., the QGP phase. Until $t \approx 20\,\mathrm{fm}/c$, the massive production of mesons leads to a strong consumption of $q/\bar{q}$. As a consequence, the decrease in the radius of the sphere is strong at these moments. Then, between 20 and 110 fm/$c$, this decrease is more reduced and seems to be almost linear. This behavior is explained by the diminution of the $q/\bar{q}$ consumption. After 110 fm/$c$, the radius stagnates until the total hadronization, about 20 fm/$c$ later. Moreover, the temperature and the densities $\rho_{u,d}$ of the QGP phase are rather constant (Fig. 35). Its average temperature is close to 250 MeV, even if variations are observable. At the opposite, the system's dynamics outside the sphere is completely different. This part of the system is composed of the mesons and baryons that left the QGP phase. The reactions $q + \bar{q} \to M + M$ involving light particles are particularly exothermic [32]. Therefore, the produced mesons, notably pions, can have strong velocities [Fig. 36(b)]. Thus, the expansion of the phase constituted by these particles is rapid. Because of this dilatation, the hadrons gradually cool down when $r$ and time increase. Thus, the dilution leads to an exponential decrease in the mean temperature and densities $\rho_{u,d}$ of the system (Fig. 35).

Concerning the collisions, Figs. 33 and 34 and Table XII make it possible to study them according to several aspects.

TABLE XI. Final composition of the system.

| Particle | $\pi^-$ | $\pi^0$ | $\pi^+$ | $\eta$ | $K^-$ | $K^+$ | $K^0$ | $\bar{K}^0$ | Neutron | Proton | $\Sigma^-$ | $\Sigma^+$ |
|---|---|---|---|---|---|---|---|---|---|---|---|---|
| No. | 84 | 64 | 72 | 3 | 3 | 9 | 6 | 7 | 9 | 17 | 2 | 3 |

In this simulation, we counted 559 collisions: ≈63% elastic and ≈37% inelastic. According to Fig. 34, the collisions preferentially occur in the first moments of the simulation, until 10 fm/$c$. There, the elastic collisions dominate the inelastic ones because of the strong temperatures. Indeed, as noted in Refs. [94], reactions as $q + \bar{q} \to q + \bar{q}$, $q + q \to q + q$, and $\bar{q} + \bar{q} \to \bar{q} + \bar{q}$ have stronger cross sections than $q + \bar{q} \to M + M$ when $T > 280\,\mathrm{MeV}$. However, this inelastic process is very present: It permits the massive mesonization observed in Fig. 32(b). Between 10 and 80 fm/$c$, because of the diminution of the population in the QGP phase, the collision rate strongly decreases but stays rather constant. As seen previously, the temperature of the QGP phase is almost constant. Therefore, as with $t < 10\,\mathrm{fm}/c$, the elastic reactions dominate the inelastic ones until 80 fm/$c$. After that, the number of particles forming the QGP phase is low. This leads to a strong reduction of the probability of interaction between two particles in this phase, as with the simulation of Sec. V B.

Figure 33 confirms these observations, with the spatial distribution of the collisions. The inelastic collisions (black dots) occur in the QGP phase, but near its surface. There the temperature is lower than in the center: These conditions are more favorable for $q + \bar{q} \to M + M$. However, endothermic reactions as $q + q \to \bar{q} + B$ are not concerned by this remark. They correspond to the inelastic reactions visible in Fig. 33 near the center of the system. Moreover, the elastic collisions occur in the whole QGP phase. It notably concerns the elastic reactions between quarks and/or antiquarks. However, elastic reactions are also observable outside of this phase: First, they are processes as $M + M \to M + M$, and second, $M + B \to M + B$ and $B + B \to B + B$ (Table XII). The

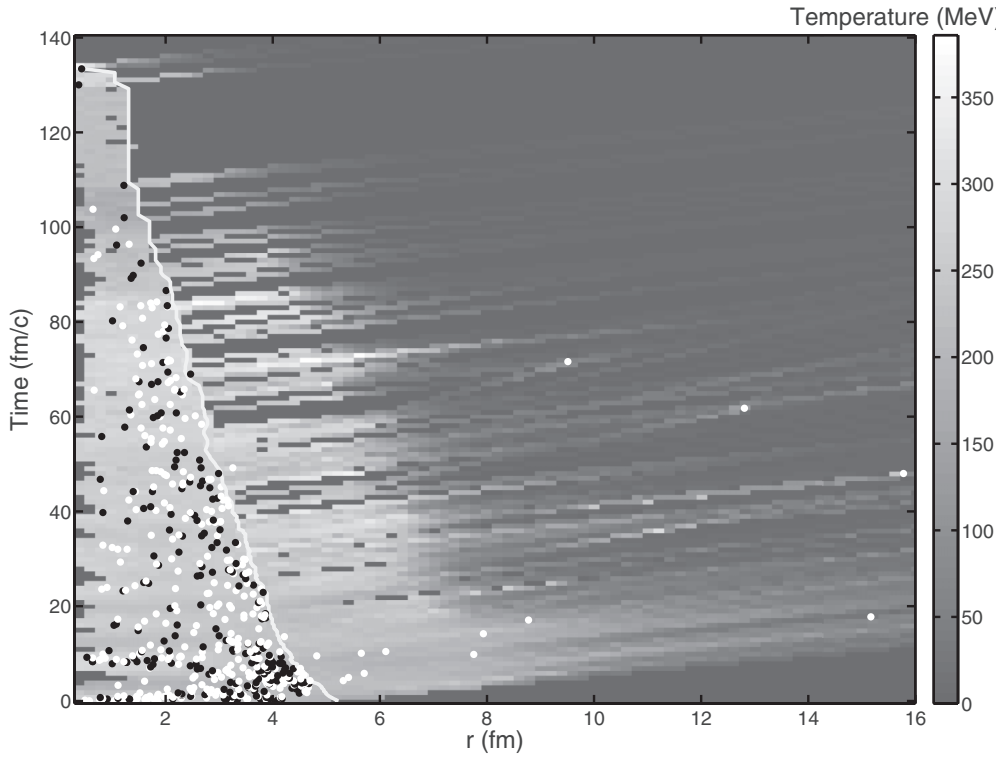


FIG. 33. Temperature according to the distance from the center of the system and according to time. The white curve marks the radius of the sphere (limit of the QGP phase). The white dots correspond to elastic collisions, and the black dots correspond to inelastic ones.

domination of $M + M \rightarrow M + M$, compared to the two other ones, is explained by the strong production of mesons. As a consequence, the meeting between two mesons is highly more probable than the $M, B$ or the $B, B$ meeting, independently of the cross sections associated with these elastic processes.

Table XII presents the occurrence of all the processes treated in the simulation. Among the 559 collisions, $q + \bar{q} \rightarrow q + \bar{q}$ reactions represent more than a quarter. $q + \bar{q} \rightarrow M + M$ corresponds to less than 20%. We observed in Sec. V B that the mesonization ended early, but this observation is not confirmed here. Indeed, antiquarks are found in the system until the total hadronization. As a consequence, the high temperatures met in this simulation affect the $q + \bar{q} \rightarrow M + M$ process in a non-negligible way. Nevertheless, these inelastic reactions were not disturbed by their reverse ones, $M + M \rightarrow q + \bar{q}$, because they intervened only one time. $q + \bar{q} \rightarrow M + M$ remains the privileged way to produce mesons, significantly more than $q + q \rightarrow M + D$. However, this conclusion can depend on the initial ratio between quarks and antiquarks. Moreover, the mesons mainly interact with other particles by elastic reactions, via $M + M \rightarrow M + M$, $q + M \rightarrow q + M$, or $\bar{q} + M \rightarrow \bar{q} + M$, but rarely by inelastic ones, as $q + M \rightarrow \bar{q} + D$ or $M + D \rightarrow \bar{q} + B$. It explains the constant growth of the mesons' population [Fig. 32(b)].

Concerning the other reactions quoted in Table XII, even if $q + \bar{q} \rightarrow q + \bar{q}$ strongly intervenes, $q + q \rightarrow q + q$ and $\bar{q} + \bar{q} \rightarrow \bar{q} + \bar{q}$ are also present. Their occurrences are several times lower than the one of the $q/\bar{q}$ scattering, because their cross sections are more reduced [48,94]. On one hand, the cross sections of $q + q \rightarrow q + q$ and $\bar{q} + \bar{q} \rightarrow \bar{q} + \bar{q}$ are similar at

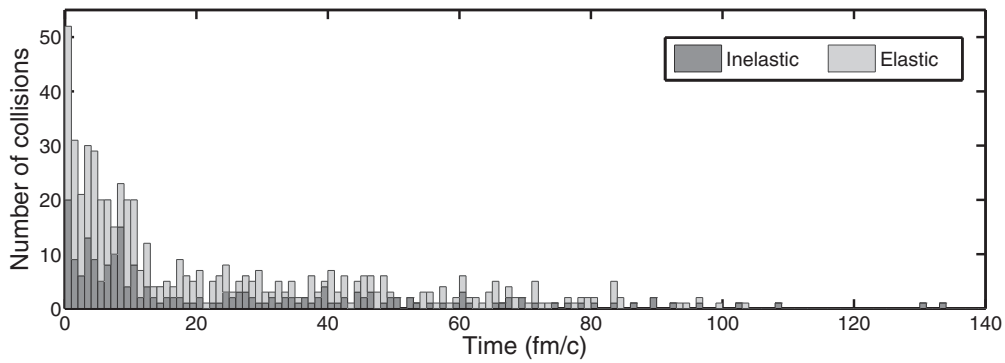


FIG. 34. Number of elastic and inelastic collisions according to time.

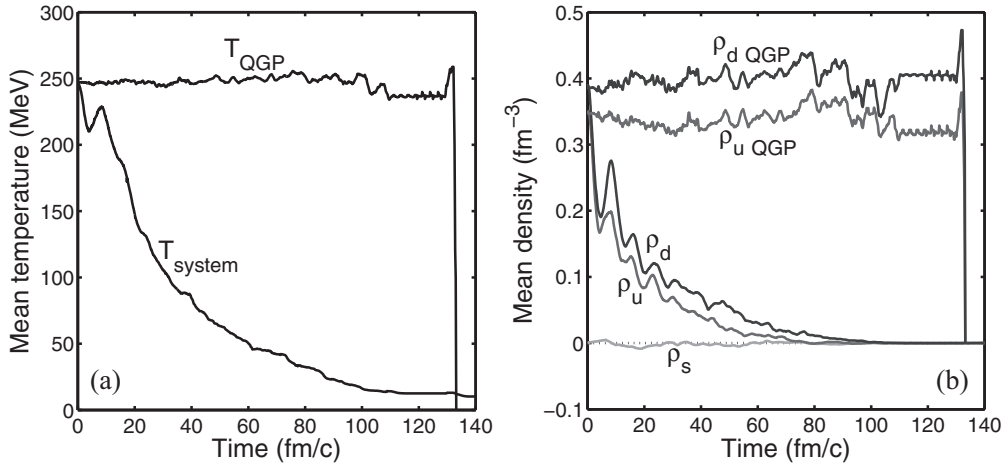


FIG. 35. (a) Mean temperatures and (b) mean densities in the whole system and in the QGP phase.

moderate densities. On the other hand, the initial ratio between matter and antimatter is equal to two. It explains why the occurrence of $q + q \rightarrow q + q$ is about twice the one of $\bar{q} + \bar{q} \rightarrow \bar{q} + \bar{q}$.

We saw that the production of diquarks cannot be neglected in this simulation. Among the inelastic processes studied in Ref. [94], the reactions $q + q \rightarrow M + D$ are the ones that produce diquarks in the more notable way (Table XII). This remark is particularly true because the reverse reactions $M + D \rightarrow q + q$ did not occur during the simulation. However, the contribution of $q + M \rightarrow \bar{q} + D$ is weak, because of low cross sections, notably compared to $\bar{q} + D \rightarrow q + M$ [94].

Concerning the baryonization, $M + D \rightarrow \bar{q} + B$ can also be neglected for the same reason. As expected in Sec. II D, the three dominant processes allowing the creation of baryons are $D + D \rightarrow q + B$, $q + D \rightarrow M + B$, and $q + q \rightarrow \bar{q} + B$. In this simulation, they give similar contributions. The baryons' production via $D + D \rightarrow q + B$ was permitted by the non-negligible population of diquarks, by interesting cross sections [94] and by the relative high temperatures in the QGP phase. Indeed, this endothermic process needs such temperatures to intervene. This argument is also valid with $q + q \rightarrow \bar{q} + B$. However, one notes that $q + B \rightarrow D + D$ is not negligible. Thus, it lowers the efficiency of the baryons' production starting from two diquarks. Then, even if $\bar{q} + B \rightarrow q + q$ can be neglected, it is not the case for $\bar{q} + B \rightarrow M + D$. This one leads to limitations of the baryonization via $q + q \rightarrow \bar{q} + B$. In contrast, $q + D \rightarrow M + B$ is not bothered by the reverse reactions: $M + B \rightarrow q + D$ was not observed. Only $q + D \rightarrow q + D$ can possibly slow down the production of baryons via $q + D \rightarrow M + B$.

We turn our attention now to Fig. 36. Its purpose is to check the validity of the results. Figure 36(a) displays the evolution of the total energy, according to time. The total energy is expected to be strictly constant. However, some variations are observable; they are attributable to numerical rounding. The inclusion of the sphere does not have any direct incidence on these fluctuations. Among the simulations described in this paper, these values are the most unfavorable ones. However, the variations are always lower than 0.8%. Furthermore, after some oscillations until 40 fm/$c$, the values stabilize at 0.5%. Such a value is acceptable; it is slightly higher than the variations

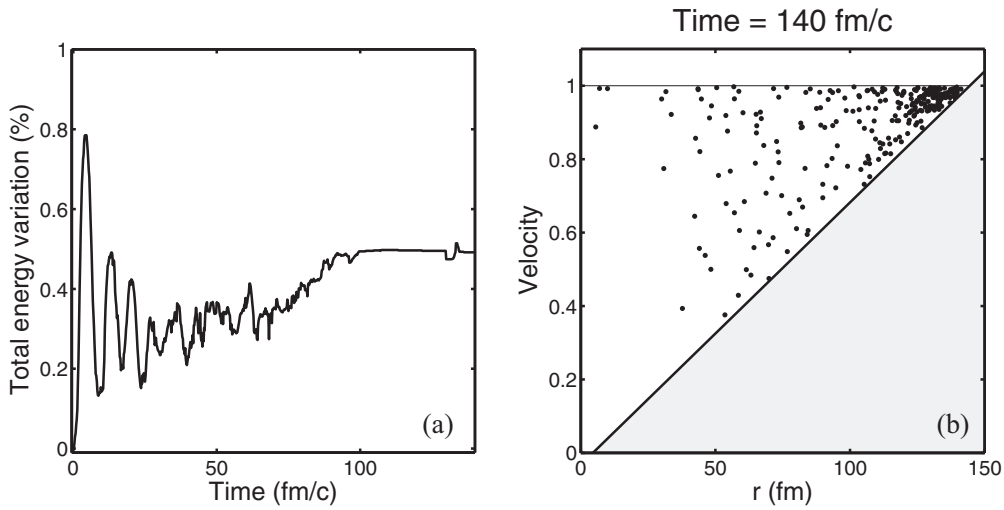


FIG. 36. (a) Fluctuations of the total energy according to time and (b) final velocities of the particles.

TABLE XII. Occurrence of each type of collision.

| | | | | | |
|---|---|---|---|---|---|
| $q + \bar{q} \to q + \bar{q}$ | 147 | $q + D \to M + B$ | 14 | $D + D \to D + D$ | 3 |
| $q + \bar{q} \to M + M$ | 106 | $\bar{q} + M \to \bar{q} + M$ | 14 | $M + B \to M + B$ | 3 |
| $q + q \to q + q$ | 59 | $q + B \to D + D$ | 10 | $B + B \to B + B$ | 2 |
| $\bar{q} + \bar{q} \to \bar{q} + \bar{q}$ | 36 | $q + M \to \bar{q} + D$ | 7 | $\bar{q} + B \to q + q$ | 1 |
| $q + D \to q + D$ | 31 | $\bar{q} + B \to M + D$ | 7 | $M + M \to q + \bar{q}$ | 1 |
| $M + M \to M + M$ | 24 | $\bar{q} + D \to q + M$ | 5 | $\bar{q} + D \to \bar{q} + D$ | 0 |
| $q + q \to M + D$ | 22 | $D + B \to D + B$ | 4 | $\bar{q} + B \to \bar{q} + B$ | 0 |
| $q + M \to q + M$ | 22 | $q + B \to q + B$ | 3 | $M + D \to q + q$ | 0 |
| $D + D \to q + B$ | 17 | $M + D \to \bar{q} + B$ | 3 | $M + B \to q + D$ | 0 |
| $q + q \to \bar{q} + B$ | 15 | $M + D \to M + D$ | 3 | | |

announced in Ref. [80]. They can be reduced if one increases the precision of the numerical calculations, but at the price of an extension of the calculation time.

Figure 36(b) displays the velocities of the particles, according to the distance from the center of the system. The data are established at $t = 140\,\mathrm{fm}/c$, i.e., in the end of the simulation. The horizontal line, for which the velocity is equal to 1, marks the speed of light. Because of strong initial momenta and because of exothermic reactions, a significant part of the particles have strong velocities, close to 1. Moreover, we saw that the remote interaction between the particles can be neglected, notably because of its limited range. In other words, once the final particles (mesons and baryons) are produced, their velocities are not expected to vary until the end of the simulation. This leads us to consider them as free particles. With this hypothesis, a diagonal line is traced in Fig. 36(b): It materializes the limit of causality in the graph. The shifting of this line according to the $r$ axis takes into account the initial radius of the system, about 4.5 fm. Particles on the right of this line would be noncausal, because they would be too far from the center of the system in comparison to their velocities. Such unphysical behavior was not observed in the results. It would have been the sign of failures of the algorithm.

Another test of the consistency of the results concerns the notions of kinetic and chemical equilibrium (Fig. 37 and Table XIII). In Fig. 37(a), I analyze the distribution of the quarks/antiquarks and diquarks at $t = 10\,\mathrm{fm}/c$, i.e., when the population of diquarks is maximal. In fact, the spectra give a vision of the QGP phase. They indicate that the studied species seem to have reached kinetic equilibrium for a temperature $T = 250\,\mathrm{MeV}$. This temperature corresponds nicely to the one of the QGP phase [Fig. 35(a)]. Table XII indicates that the number of elastic reactions involving quarks/antiquarks and diquarks is strong enough to realize the observed kinetic equilibration of these particles.

Moreover, the reasoning done in Sec. V C about the hadrons present in the final state is also applicable here. In that way, I plot the associated distributions in Fig. 37(b). The aspect of this figure recalls the energy spectra visible in Refs. [67,116]. The found results also show that the kinetic equilibration was performed in the simulation. As in Sec. V C, a part of the hadrons are produced in the sphere when the QGP phase is at kinetic equilibrium [Fig. 37(a)]. The ones that are created early, notably mesons, certainly undergo different conditions, as the high temperatures visible in Fig. 30(b). However, I also evoke their thermalization by means of the non-negligible elastic reactions $M + M \to M + M$, $q + M \to q + M$, and $\bar{q} + M \to \bar{q} + M$ (Table XII). However, some imperfections are found at high energies. Concerning the pions, these imperfections correspond to a deficit when $E > 1.4\,\mathrm{GeV}$. The

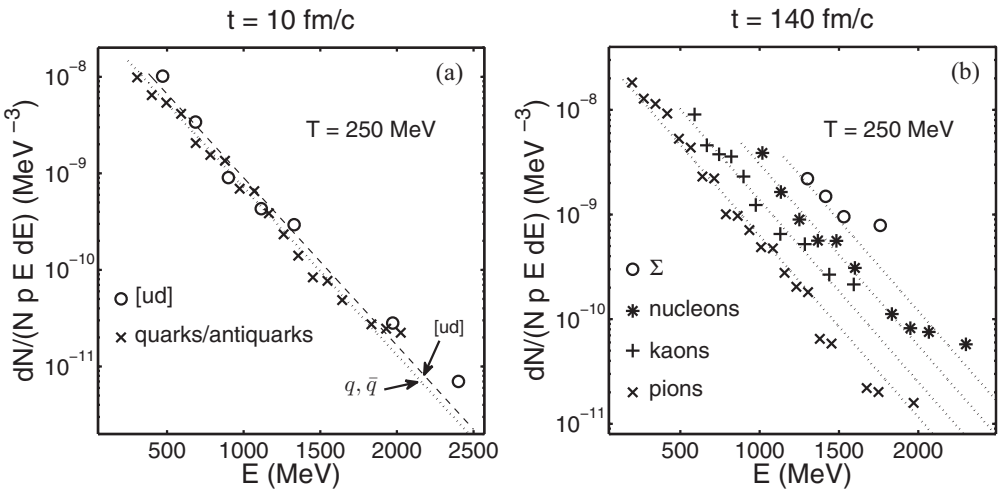


FIG. 37. (a) Energy distributions of the quarks/antiquarks and diquarks at $t = 10\,\mathrm{fm}/c$ and (b) energy distributions of the hadrons in the final state.

TABLE XIII. Number $N$ of hadrons found in the simulation and theoretical estimations $N_{eq}$.

| Particle | Pion | Kaon | Nucleon | $\Sigma$ |
|---|---|---|---|---|
| $N$ | 220 | 25 | 26 | 5 |
| $N_{eq}$ | 252 | 167 | 51 | 28 |
| $N_{eq}$ with Eq. (34) | 200 | 140 | 45 | 24 |

limited number of pions at such energies constitutes a possible explanation. This argument is also applicable to explain the imperfections found for the baryons. However, for them, I may evoke the lack of interactions with the QGP phase, which is attested by the low number of elastic reactions involving baryons (Table XII).

The chemical equilibrium is studied through Table XIII, as in Sec. V C. First, the number of created pions corresponds well to the theoretical predictions. Then, the number of baryons appears to be rather weak. It can be explained by the initial conditions and more precisely by the initial matter/antimatter ratio (Table X). In fact, the populations of the treated species, except the pions, seem to be underestimated. It constitutes a sign that the approach involving $2 \to 2$ reactions should be completed by multiparticle reactions, making it possible to modify (to increase in this case) the total number of particles. It should notably concern $2 \to 3$ reactions. Moreover, the number of kaons is strongly lower than the $N_{eq}$ predictions, approximately by a factor of 6. This observation can be extended to the $\Sigma$ baryons. Thus, it confirms the results of Sec. V C, in which the strangeness production was also too weak compared to statistical estimations. In the present simulation, higher temperatures were considered, but they do not lead to the expected production. Clearly, the strangeness creation is possible, but it only concerns a few reactions. Indeed, the kinematic threshold sometimes prevents such a production. In addition, when this criterion is satisfied, the reactions that can form $s/\bar{s}$, kaons, or hyperons remain dominated by processes creating light particles. One can imagine two ways to reach the required number of strange particles: higher temperatures or inclusion of strange matter in the initial composition. In fact, these solutions indicate that the chemical equilibration of the strange particles is strongly related to the initial conditions. These results lead us to quote the observation done in Ref. [104], in the framework of quark/gluon simulations. It is indicated that the chemical equilibration depends on the initial conditions, whereas kinetic equilibration appears to be almost independent of them, as observed in my work.

## VII. CONCLUSIONS

In this paper, I presented a dynamical model devoted to studying the cooling of a quark-antiquark plasma. To reach this objective, the NJL model was used, completed by the inclusion of a Polyakov loop, forming the PNJL model. I recalled some notions about these models and presented some results as the modeling of quarks, mesons, diquarks, and baryons [45] and the cross-section calculations [32,44,94]. Then, I detailed the algorithm. I described how the external parameters felt by each particle are estimated. More precisely, I considered the temperature and the densities $\rho_f$ treated as local parameters. I explained the collision algorithm, in which 60 types of reactions were referenced, involving quarks, mesons, diquarks, baryons, and their antiparticles. In my approach, the cross sections were evaluated according to $\sqrt{s}, T, \rho_f$, being aware of the interest to take into account fully the contributions of these parameters in the cross-section calculations.

I also presented the equations of motion, based on a relativistic molecular dynamics description, and I interpreted them in the framework of the (P)NJL models. I discovered a remote interaction between the particles. I investigated the properties of this interaction between quarks numerically. An attractive force was found, whose effects mainly concern slow quarks, at low and moderate temperatures. The inclusion of the Polyakov loop makes it possible to increase the temperature range in which this force can intervene in a notable way. However, this interaction has a limited influence in hot systems, involving rapid particles. Also, it has a reduced range, i.e., a few femtometers in my description. However, it should be interesting to investigate this remote interaction in the framework of future simulations involving different conditions.

Moreover, I compared NJL and PNJL complete simulations. The PNJL model made it possible to obtain better results, i.e., a more efficient hadronization. This observation was explained by the shifting of the temperatures caused by the inclusion of the Polyakov loop. This one affects the value of the pseudocritical temperature $T_c$ and also the Mott temperatures of the composite particles. Thus, it leads to an extension of the domain of stability of these particles towards higher temperatures. Also, it indirectly concerns the cross sections: The optimal temperature of the mesonization reaction that creates pions is shifted from 230 MeV in a pure NJL description towards 280 MeV in the PNJL one. It induces a better mesonization of the $q/\bar{q}$ system under the conditions of the performed simulations. Indeed, in the PNJL model, the mesonization was possible even in hot zones ($T \leqslant 280$ MeV), whereas it was not the case for NJL.

However, the hadronization was not complete in these tests, even with the PNJL model. The relative weakness of the baryonization reactions was evoked to explain this limitation. On this occasion, the necessity of a long-range interaction between quarks was underlined. I showed the possibility to mimic such an interaction by the inclusion of a sphere, whose role was to confine the quarks/antiquarks and the diquarks until their hadronization. Even if box calculations are particularly interesting in the frameworks of such works [73,102,103], I concede that the sphere should be considered as a first step. The description of long-range interactions should be developed in the (P)NJL models.

Then, with this confining sphere, I described the evolution of two simulations, until their complete hadronization. The first simulation involved moderate temperatures, whereas the second one considered more particles and initial temperatures exceeding 300 MeV. The two simulations confirmed the scenario proposed in Ref. [94]. At high temperatures, elastic reactions between $q/\bar{q}$ dominate. When $T \leqslant 280$ MeV,

$q + \bar{q} \rightarrow M + M$ allows a massive mesonization, producing a great number of pions in a short amount of time. This mesonization consumes enough antiquarks to permit the formation of baryons. In the second simulation, the high temperatures and densities allowed a notable production of diquarks, by reactions as $q + q \rightarrow M + D$. These particles acted as intermediate states to facilitate the baryonization. I noted that the baryons were preferentially created by $D + D \rightarrow q + B, q + q \rightarrow \bar{q} + B$, and $q + D \rightarrow M + B$, with an advantage for the last one.

We saw that one effect of the sphere was to stabilize the temperature and the density of the QGP phase. Furthermore, the sphere allowed the systems to evolve towards kinetic equilibration in a more efficient way than in the sphereless simulations. More precisely, the simulations that used the sphere reached the kinetic equilibrium. Moreover, in these simulations, we observed the production of strange particles starting from light quarks/antiquarks. However, this production was insufficient in comparison to statistical calculations. Also, for the two simulations in which the hadronization was complete, the required time was found to be higher than expected in the literature [118].

A possible way to correct these two limitations could be the inclusion of multiparticle reactions as $2 \rightarrow 3$, $3 \rightarrow 2$, and $3 \rightarrow 3$ in my work. Indeed, concerning the time scales for the hadronization, these reactions could make it possible to increase the collision rate, notably in the beginning of the simulation. More precisely, the initial conditions correspond to high concentrations of particles, so reactions involving three incoming particles should intervene in a non-negligible way at this moment. Moreover, concerning the chemical equilibration, the influence of the multiparticle reactions on the equilibration of quark/gluon systems was shown, e.g., in Refs. [102,103]. This observation could be extrapolated to my simulations. Furthermore, I can also explain the insufficient strangeness production by the absence of gluons (as dynamical particles) in my modeling. Indeed, they are expected to play an important role in the creation of strange matter, via reactions as $g + g \rightarrow s + \bar{s}$ [119,120].

Concerning the possible evolutions of this work, apart from the ones already mentioned above, I may suggest the inclusion of heavy mesons as vectorial ones. In the same way, it could be interesting to take into account decuplet baryons [45]. Obviously, such a work requires an extension of the cross-section calculations performed in Ref. [94], and a treatment of the decays of the instable particles, as the one initiated in Ref. [80] for the pseudoscalar mesons. Other possibilities concern the inclusion of antiparticles as antidiquarks and antibaryons in the simulations to investigate their contribution, especially at moderate densities.

## APPENDIX A: DETERMINATION OF THE TEMPERATURE

In a nonrelativistic regime, the temperature of an ideal gas is obtained, at the thermal equilibrium, by the equipartition theorem,

$$\langle E_K \rangle_{\text{n.r.}} = \tfrac{3}{2}\, k_B\, T, \tag{A1}$$

where $\langle E_K \rangle_{\text{n.r.}}$ is the mean value of the nonrelativistic kinetic energy. A general formulation of this theorem explains that for each degree of freedom $\phi_i$ (quadratic variable in the writing of the energy) the following relation is satisfied [106]:

$$\left\langle \phi_i \, \frac{\partial E}{\partial \phi_i} \right\rangle = k_B\, T. \tag{A2}$$

In a relativistic formulation, $\langle E \rangle = \langle \sqrt{p_x^2 + p_y^2 + p_z^2 + m^2} \rangle$. One considers then three configurations:

(i) *Nonrelativistic regime*, i.e., $(\vec{p})^2 \ll m^2$, leading to the well-known approximation

$$\langle E \rangle \approx \left\langle \frac{p_x^2 + p_y^2 + p_z^2}{2m} + m \right\rangle \equiv \langle E_K \rangle_{\text{n.r.}} + \langle m \rangle . \tag{A3}$$

According to Eqs. (A2) and (A3), $\langle p_i \, \frac{\partial E}{\partial p_i} \rangle = \langle \frac{p_i^2}{m} \rangle = k_B\, T$, where $i = x,y,z$; it makes it possible to find Eq. (A1) again.

(ii) *Ultrarelativistic regime* [113], where $(\vec{p})^2 \gg m^2$. In this case

$$\langle E \rangle \approx \left\langle \sqrt{p_x^2 + p_y^2 + p_z^2} \right\rangle \equiv \langle E_K \rangle_{\text{u.r.}}. \tag{A4}$$

In the same way, one finds $\langle p_i \, \frac{\partial E}{\partial p_i} \rangle = \langle \frac{p_i^2}{\sqrt{p_x^2+p_y^2+p_z^2}} \rangle = k_B\, T$. Thus, one obtains

$$\langle E_K \rangle_{\text{u.r.}} = \left\langle \frac{p_x^2 + p_y^2 + p_z^2}{\sqrt{p_x^2 + p_y^2 + p_z^2}} \right\rangle = \sum_{i=x,y,z} \left\langle p_i \, \frac{\partial E}{\partial p_i} \right\rangle,$$

$$\text{and thus } \langle E_K \rangle_{\text{u.r.}} = 3\, k_B\, T. \tag{A5}$$

(iii) *General case.* Using the same method as in the previous cases, one considers again $\langle E \rangle = \langle \sqrt{p_x^2 + p_y^2 + p_z^2 + m^2} \rangle$. Thus, one writes

$$\left\langle p_i \, \frac{\partial E}{\partial p_i} \right\rangle = \left\langle \frac{p_i^2}{\sqrt{p_x^2 + p_y^2 + p_z^2 + m^2}} \right\rangle = k_B\, T. \tag{A6}$$

One performs the summation of the contributions of the three components $x,y,z$, and one obtains Eq. (27) [106,112,113]

$$\left\langle \frac{(\vec{p})^2}{E} \right\rangle = 3 k_B\, T. \tag{A7}$$

## APPENDIX B: ELEMENTS OF KINEMATICS

The collisions between the two incoming particles 1, 2 and the two outgoing ones 3, 4, are schematized in Fig. 38 [94].

$p_i$ is the four-momentum of the concerned particle. $E_i = \sqrt{(\vec{p}_i)^2 + m_i^2}$ is its associated energy, i.e., the 0th component of this four-vector. I use the symbol * hereafter to specify that the variables are expressed in the center-of-mass reference frame of the incoming particles. The relations between the energies,

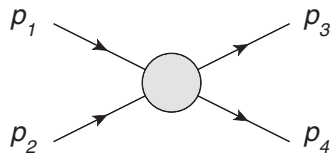


FIG. 38. Schematization of a $2 \to 2$ collision.

the momenta and the Mandelstam variable $s$ are then written as [121]

$$\begin{aligned}
E_1^* &= \frac{s + m_1^2 - m_2^2}{2\sqrt{s}}, \\
\|\vec{p}_1^*\| &= \frac{\sqrt{[s-(m_1+m_2)^2][s-(m_1-m_2)^2]}}{2\sqrt{s}}, \\
E_2^* &= \frac{s - m_1^2 + m_2^2}{2\sqrt{s}}, \\
\vec{p}_2^* &= -\vec{p}_1^*, \\
E_3^* &= \frac{s + m_3^2 - m_4^2}{2\sqrt{s}}, \\
\|\vec{p}_3^*\| &= \frac{\sqrt{[s-(m_3+m_4)^2][s-(m_3-m_4)^2]}}{2\sqrt{s}}, \\
E_4^* &= \frac{s - m_3^2 + m_4^2}{2\sqrt{s}}, \\
\vec{p}_4^* &= -\vec{p}_3^*,
\end{aligned} \tag{B1}$$

where the Mandelstam variables $s$, $t$, $u$ are defined as

$$\begin{aligned}
s &= (p_1 + p_2)^2 = (p_3 + p_4)^2, \\
t &= (p_3 - p_1)^2 = (p_4 - p_2)^2, \\
u &= (p_4 - p_1)^2 = (p_3 - p_2)^2.
\end{aligned} \tag{B2}$$

The bounds of the integral Eq. (20) are associated with the Mandelstam variable $t$, with

$$t_\pm = m_1^2 + m_3^2 - 2\,E_1^*\,E_3^* \pm 2\|\vec{p}_1^*\|\,\|\vec{p}_3^*\|. \tag{B3}$$

## APPENDIX C: GEOMETRICAL CALCULATIONS DEVOTED TO THE COLLISIONS

### 1. Impact parameter

The momenta of the incoming particles are initially expressed in the laboratory frame. Therefore, the first step in estimating the impact parameter $b^*$ is to apply a Lorentz boost on these momenta to work in the center-of-mass reference frame of these two particles,

$$\begin{aligned}
\vec{p}_1^* &= \vec{p}_1 + \vec{v}_{\text{c.m.}} \left[ (\Gamma - 1)\,\frac{\vec{p}_1 \cdot \vec{v}_{\text{c.m.}}}{\|\vec{v}_{\text{c.m.}}\|^2} - \Gamma\, E_1 \right], \\
E_1^* &= \Gamma(E_1 - \vec{p}_1 \cdot \vec{v}_{\text{c.m.}}),
\end{aligned} \tag{C1}$$

where $\vec{v}_{\text{c.m.}}$ is the velocity of the center of mass in the laboratory frame,

$$\vec{v}_{\text{c.m.}} = \frac{\vec{p}_1 + \vec{p}_2}{E_1 + E_2}, \tag{C2}$$

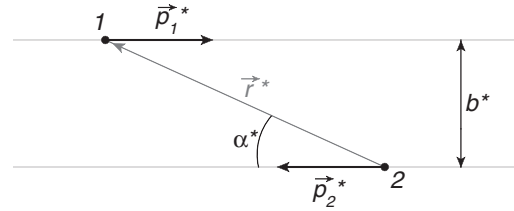


FIG. 39. Determination of the impact parameter $b^*$.

and the Lorentz factor is written as

$$\Gamma = \frac{1}{\sqrt{1 - (v_{\text{c.m.}}/c)^2}}, \tag{C3}$$

in which the speed of light $c$ is set equal to 1. Then Eq. (C1) is adapted for the momentum of the incoming particle 2. The same procedure is applied to the positions of these particles 1 and 2 to express them in their center-of-mass reference frame. One obtains then $\vec{r}_1^*$ and $\vec{r}_2^*$, respectively. Now, one defines $\vec{r}^* = \vec{r}_1^* - \vec{r}_2^*$ and $\vec{p}^* = \vec{p}_2^* - \vec{p}_1^*$. Because $\vec{p}_1^* + \vec{p}_2^* = \vec{0}$, the choice $\vec{p}^* = \vec{p}_2^*$ gives the same results in the calculation performed hereafter.

With Fig. 39, Eq. (C4) are found by geometrical considerations:

$$\cos(\alpha^*) = \frac{\vec{r}^* \cdot \vec{p}^*}{\|\vec{r}^*\|\ \|\vec{p}^*\|}, \quad \sin(\alpha^*) = \frac{b^*}{\|\vec{r}^*\|}. \tag{C4}$$

Using the formula $\sin[\cos^{-1}(x)] = \sqrt{1 - x^2}$, the impact parameter $b^*$ is expressed, as in Ref. [67], by the relation

$$b^* = \sqrt{\|\vec{r}^*\|^2 - \left(\frac{\vec{r}^* \cdot \vec{p}^*}{\|\vec{p}^*\|}\right)^2}. \tag{C5}$$

The first equation of Eq. (C4) indicates if the particles are approaching [$\cos(\alpha^*) \geqslant 0$] or are moving away [$\cos(\alpha^*) < 0$]. This information cannot be supplied by Eq. (C5). If $\cos(\alpha^*) < 0$, the collision procedure is aborted for these two particles.

### 2. Scattering angle and momenta of the outgoing particles

Figure 40 illustrates the applied method to calculate the scattering angle $\theta^*$, in which $\sigma$ is the cross section of the reaction $1 + 2 \to 3 + 4$. In the figure, $\vec{r}^*$ is a vector connecting the two particles 1 and 2 at the precise instant of their interaction. This one is supposed to be spatially and temporally punctual. $\vec{p}_3^*$ and $\vec{p}_4^*$ are, respectively, the momenta of the outgoing particles 3 and 4. Their modulus is found with Eq. (B1).

The approach considers the hard sphere model as a starting point. But, here, the sum of the radii of particles 1 and 2 is replaced by $\sqrt{\sigma/\pi}$. Then, particle 1 becomes particle 3 after a rebound on the sphere visible in Fig. 40, according to

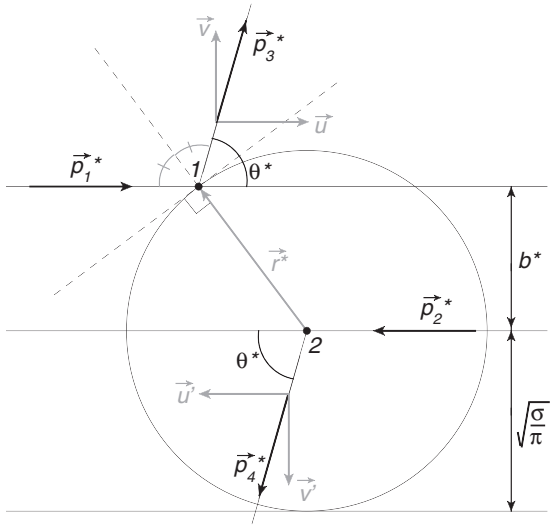


FIG. 40. Method to estimate the scattering angle $\theta^*$.

Snell-Descartes' law of reflection, whereas particle 2 becomes particle 4. Geometrical considerations make it possible to find the expression of the scattering angle $\theta^*$ :

$$\theta^* = \pi - 2\ \sin^{-1}(b\sqrt{\pi/\sigma}). \tag{C6}$$

The coordinates of the vectors $\vec{p}_3^{\,*}$ and $\vec{p}_4^{\,*}$ are then fully determinable with this angle: The vector $\vec{p}_3^{\,*}$ is projected in the $(\vec{u},\ \vec{v})$ basis, where one defines

$$\vec{u} = \frac{\vec{p}_1^{\,*}}{\|\vec{p}_1^{\,*}\|}, \quad \vec{v} = \frac{\vec{r}^{\,*} - (\vec{r}^{\,*}\cdot\vec{u})\,\vec{u}}{\|\vec{r}^{\,*} - (\vec{r}^{\,*}\cdot\vec{u})\,\vec{u}\|}. \tag{C7}$$

The procedure is similar for $\vec{p}_4^{\,*}$, or one uses $\vec{p}_4^{\,*} = -\vec{p}_3^{\,*}$ (B1). Finally, a Lorentz boost is applied to these momenta to express them in the laboratory frame.


[1] M. J. Tannenbaum, arXiv:1302.1833.
[2] C. DeTar, in *Quark-Gluon Plasma 2*, edited by R. Hwa (World Scientific, Singapore, 1995), pp. 1–50.
[3] H. Meyer-Ortmanns, Rev. Mod. Phys. **68**, 473 (1996).
[4] F. Karsch, Lect. Notes Phys. **583**, 209 (2002).
[5] E. Laermann and O. Philipsen, Annu. Rev. Nucl. Part. Sci. **53**, 163 (2003).
[6] P. Petreczky, J. Phys. G: Nucl. Part. Phys. **39**, 093002 (2012).
[7] Z. Fodor, Nucl. Phys. A **715**, 319 (2003).
[8] A. Dumitru, R. D. Pisarski, and D. Zschiesche, Phys. Rev. D **72**, 065008 (2005).
[9] Y. Nambu and G. Jona-Lasinio, Phys. Rev. **122**, 345 (1961).
[10] Y. Nambu and G. Jona-Lasinio, Phys. Rev. **124**, 246 (1961).
[11] T. Hatsuda and T. Kunihiro, Phys. Lett. B **206**, 385 (1988).
[12] T. Hatsuda and T. Kunihiro, Phys. Rep. **247**, 221 (1994).
[13] V. Bernard, U. G. Meissner, and I. Zahed, Phys. Rev. D **36**, 819 (1987).
[14] V. Bernard, U. G. Meissner, and I. Zahed, Phys. Rev. Lett. **59**, 966 (1987).
[15] V. Bernard and U. G. Meissner, Nucl. Phys. A **489**, 647 (1988).
[16] V. Bernard, R. L. Jaffe, and U. G. Meissner, Nucl. Phys. B **308**, 753 (1988).
[17] S. P. Klevansky, Rev. Mod. Phys. **64**, 649 (1992).
[18] S. Klimt, M. Lutz, U. Vogl, and W. Weise, Nucl. Phys. A **516**, 429 (1990).
[19] U. Vogl, M. Lutz, S. Klimt, and W. Weise, Nucl. Phys. A **516**, 469 (1990).
[20] U. Vogl and W. Weise, Prog. Part. Nucl. Phys. **27**, 195 (1991).
[21] M. Lutz, S. Klimt, and W. Weise, Nucl. Phys. A **542**, 521 (1992).
[22] J. Bijnens, Phys. Rep. **265**, 370 (1996).
[23] M. Buballa, Phys. Rep. **407**, 205 (2005).
[24] A. A. Osipov, B. Hiller, and J. da Providencia, Phys. Lett. B **634**, 48 (2006).
[25] A. A. Osipov, B. Hiller, J. Moreira, A. H. Blin, and J. da Providencia, Phys. Lett. B **646**, 91 (2007).
[26] K. Kashiwa, H. Kouno, T. Sakaguchi, M. Matsuzaki, and M. Yahiro, Phys. Lett. B **647**, 446 (2007).
[27] B. Hiller, J. Moreira, A. A. Osipov, and A. H. Blin, Phys. Rev. D **81**, 116005 (2010).
[28] A. Bhattacharyya, P. Deb, S. K. Ghosh, and R. Ray, Phys. Rev. D **82**, 014021 (2010).
[29] T. Matsubara, Prog. Theor. Phys. **14**, 351 (1955).
[30] D. Ebert, Lect. Notes Phys. **508**, 103 (1998).
[31] P. Rehberg and S. P. Klevansky, Ann. Phys. **252**, 422 (1996).
[32] P. Rehberg, S. P. Klevansky, and J. Hüfner, Phys. Rev. C **53**, 410 (1996).
[33] V. Bernard, U. G. Meissner, and A. A. Osipov, Phys. Lett. B **324**, 201 (1994).
[34] D. Ebert, Lect. Notes Phys. **508**, 115 (1998).
[35] M. Oettel, Ph.D. thesis, Tuebingen University, 2000.
[36] M. Oettel, R. Alkofer, and L. von Smekal, Eur. Phys. J. A **8**, 553 (2000).
[37] N. Ishii, W. Bentz, and K. Yazaki, Phys. Lett. B **318**, 26 (1993).
[38] N. Ishii, W. Bentz, and K. Yazaki, Nucl. Phys. A **587**, 617 (1995).
[39] A. Buck, R. Alkofer, and H. Reinhardt, Phys. Lett. B **286**, 29 (1992).
[40] D. Ebert, H. Reinhardt, and M. K. Volkov, Prog. Part. Nucl. Phys. **33**, 1 (1994).
[41] D. Ebert, T. Feldmann, C. Kettner, and H. Reinhardt, Int. J. Mod. Phys. A **13**, 1091 (1998).
[42] W. Bentz and A. W. Thomas, Nucl. Phys. A **696**, 138 (2001).
[43] F. Gastineau and J. Aichelin, J. Phys. G: Nucl. Part. Phys. **28**, 2017 (2002).
[44] F. Gastineau and J. Aichelin, AIP Conf. Proc. **739** 398 (2004).
[45] E. Blanquier, J. Phys. G: Nucl. Part. Phys. **38**, 105003 (2011).
[46] J. Wang, Q. Wang, and D. Rischke, Phys. Lett. B **704**, 347 (2011).
[47] C. Mu, Y. Jiang, P. Zhuang, and Y. Liu, Phys. Rev. D **85**, 014033 (2012).

[48] P. Rehberg, S. P. Klevansky, and J. Hüfner, Nucl. Phys. A **608**, 356 (1996).
[49] S. P. Klevansky, Lect. Notes Phys. **516**, 113 (1998).
[50] Y. B. He, J. Hüfner, S. P. Klevansky, and P. Rehberg, Nucl. Phys. A **630**, 719 (1998).
[51] P. Piwnicki, S. P. Klevansky, and P. Rehberg, Phys. Rev. C **58**, 502 (1998).
[52] D. S. Isert, S. P. Klevansky, and P. Rehberg, Nucl. Phys. A **643**, 275 (1998).
[53] F. Gastineau, Ph.D. thesis, Nantes University, 2002.
[54] F. Gastineau, E. Blanquier, and J. Aichelin, Phys. Rev. Lett. **95**, 052001 (2005).
[55] D. Davesne, Y. J. Zhang, and G. Chanfray, Phys. Rev. C **62**, 024604 (2000).
[56] P. Zhuang, M. Huang, and Z. Yang, Phys. Rev. C **62**, 054901 (2000).
[57] M. Bleicher *et al.*, J. Phys. G: Nucl. Part. Phys. **25**, 1859 (1999).
[58] L. D. Landau, Izv. Akad. Nauk SSSR Ser. Fiz. **17**, 51 (1953).
[59] S. Z. Belenkij and L. D. Landau, Fiz. Nauk. **56**, 309 (1955).
[60] L. D. Landau and E. M. Lifschitz, *Fluid Mechanics* (Pergamon Press, Oxford, 1959).
[61] P. F. Kolb and U. Heinz, in *Quark-Gluon Plasma 3*, edited by R. C. Hwa and X. N. Wang (World Scientific, Singapore, 2004), pp. 634–714.
[62] P. Huovinen and P. V. Ruuskanen, Annu. Rev. Nucl. Part. Sci. **56**, 163 (2006).
[63] M. Luzum and P. Romatschke, Phys. Rev. C **78**, 034915 (2008).
[64] J. Y. Ollitraut, Eur. J. Phys. **29**, 275 (2008).
[65] P. Romatschke, Int. J. Mod. Phys. E **19**, 1 (2010).
[66] R. J. M. Snellings, Nucl. Phys. A **698**, 193 (2002).
[67] S. A. Bass *et al.*, Prog. Part. Nucl. Phys. **41**, 255 (1998).
[68] H. Song, S. A. Bass, U. W. Heinz, T. Hirano, and C. Shen, Phys. Rev. Lett. **106**, 192301 (2011).
[69] R. A. Soltz, I. Garishvili, M. Cheng, B. Abelev, A. Glenn, J. Newby, L. A. Linden Levy, and S. Pratt, Phys. Rev. C **87**, 044901 (2013).
[70] W. Cassing and E. L. Bratkovskaya, Phys. Rev. C **78**, 034919 (2008).
[71] W. Cassing and E. L. Bratkovskaya, Nucl. Phys. A **831**, 215 (2009).
[72] E. L. Bratkovskaya, W. Cassing, V. P. Konchakovski, and O. Linnyk, Nucl. Phys. A **856**, 162 (2011).
[73] V. Ozvenchuk, O. Linnyk, M. I. Gorenstein, E. L. Bratkovskaya, and W. Cassing, Phys. Rev. C **87**, 024901 (2013).
[74] J. Uphoff, O. Fochler, Z. Xu, and C. Greiner, Nucl. Phys. A **855**, 444 (2011).
[75] R. Rapp, Eur. Phys. J. C **43**, 91 (2005).
[76] R. J. Fries, V. Greco, and P. Sorensen, Annu. Rev. Nucl. Part. Sci. **58**, 177 (2008).
[77] M. He, R. J. Fries, and R. Rapp, Phys. Rev. C **86**, 014903 (2012).
[78] L. Ravagli and R. Rapp, Phys. Lett. B **655**, 126 (2007).
[79] P. Rehberg, L. Bot, and J. Aichelin, Nucl. Phys. A **653**, 415 (1999).
[80] R. Marty and J. Aichelin, Phys. Rev. C **87**, 034912 (2013).
[81] A. M. Polyakov, Phys. Lett. B **72**, 477 (1978).
[82] P. N. Meisinger, M. C. Ogilvie, and T. R. Miller, Phys. Lett. B **585**, 149 (2004).
[83] K. Fukushima, Phys. Lett. B **591**, 277 (2004).
[84] Y. Hatta and K. Fukushima, arXiv:hep-ph/0311267.
[85] K. Fukushima, Phys. Part. Nucl. Lett. **8**, 838 (2011).
[86] C. Ratti, M. A. Thaler, and W. Weise, Phys. Rev. D **73**, 014019 (2006).
[87] C. Ratti, M. A. Thaler, and W. Weise, arXiv:nucl-th/0604025.
[88] S. Rossner, C. Ratti, and W. Weise, Phys. Rev. D **75**, 034007 (2007).
[89] H. Hansen, W. M. Alberico, A. Beraudo, A. Molinari, M. Nardi, and C. Ratti, Phys. Rev. D **75**, 065004 (2007).
[90] C. Ratti, S. Roessner, M. A. Thaler, and W. Weise, Eur. Phys. J. C **49**, 213 (2007).
[91] P. Costa, M. C. Ruivo, C. A. de Sousa, H. Hansen, and W. M. Alberico, Phys. Rev. D **79**, 116003 (2009).
[92] P. Costa, M. C. Ruivo, C. A. de Sousa, and H. Hansen, Symmetry **2**, 1338 (2010).
[93] Y. Sakai, T. Sasaki, H. Kouno, and M. Yahiro, PoS (Lattice 2010) 213.
[94] E. Blanquier, J. Phys. G: Nucl. Part. Phys. **39**, 105003 (2012).
[95] I. A. Shovkovy, Found. Phys. **35**, 1309 (2004).
[96] K. Rajagopal and F. Wilczek, in *At the Frontier of Particle Physics / Handbook of QCD*, edited by M. Shifman, Vol. 3 (World Scientific, Singapore, 2001), pp. 2061–2151.
[97] F. Gastineau, R. Nebauer, and J. Aichelin, Phys. Rev. C **65**, 045204 (2002).
[98] H. J. Warringa, D. Boer, and J. O. Andersen, Phys. Rev. D **72**, 014015 (2005).
[99] S. B. Rüster, V. Werth, M. Buballa, I. A. Shovkovy, and D. Rischke, Phys. Rev. D **72**, 034004 (2005).
[100] D. Blaschke, S. Fredriksson, H. Grigorian, A. M. Öztaş, and F. Sandin, Phys. Rev. D **72**, 065020 (2005).
[101] P. Maris, Few-Body Syst. **32**, 41 (2002).
[102] Z. Xu and C. Greiner, Phys. Rev. C **71**, 064901 (2005).
[103] B. Zhang and W. A. Wortman, J. Phys.: Conf. Ser. **312**, 012017 (2011).
[104] Z. Xu, L. Cheng, A. El, K. Gallmeister, and C. Greiner, J. Phys. G: Nucl. Part. Phys. **36**, 064035 (2009).
[105] X. M. Xu, J. Phys.: Conf. Ser. **432**, 012009 (2013).
[106] R. C. Tolman, Phys. Rev. **11**, 261 (1918).
[107] A. Komar, Phys. Rev. D **18**, 1887 (1978).
[108] P. G. Bergmann and A. Komar, Gen. Relativ. Gravitation **14**, 731 (1982).
[109] A. Komar, Gen. Relativ. Gravitation **27**, 1185 (1995).
[110] A. Komar, Gen. Relativ. Gravitation **28**, 379 (1996).
[111] J. A. McLennan, J. Stat. Phys. **57**, 887 (1989).
[112] J. Dunkel and P. Hänggi, Phys. Rep. **471**, 1 (2009).
[113] T. Koide and T. Kodama, Phys. Rev. E **83**, 061111 (2011).
[114] G. Chacón-Acosta, L. Dagdug, and H. A. Morales-Técotl, Phys. Rev. E **81**, 021126 (2010).
[115] A. Aliano, L. Rondoni, and G. P. Morriss, Eur. Phys. J. B **50**, 361 (2005).
[116] M. Belkacem *et al.*, Phys. Rev. C **58**, 1727 (1998).
[117] P. Braun-Munzinger, J. Stachel, J. P. Wessels, and N. Xu, Phys. Lett. B **365**, 1 (1996).
[118] J. D. Bjorken, Phys. Rev. D **27**, 140 (1983).
[119] J. Rafelski and B. Müller, Phys. Rev. Lett. **48**, 1066 (1982).
[120] P. Koch, B. Müller, and J. Rafelski, Phys. Rep. **142**, 167 (1986).
[121] V. I. Borodulin, R. N. Rogalyov, and S. R. Slabospitsky, arXiv:hep-ph/9507456.